8-15-2017

Eddy Heat Flux Across the Antarctic Circumpolar Current Estimated from Sea Surface Height Standard Deviation

Annie Foppert
University of Rhode Island

Kathleen A. Donohue
University of Rhode Island, kdonohue@uri.edu

D. Randolph Watts
University of Rhode Island, randywatts@uri.edu

Karen Tracey
University of Rhode Island

Citation/Publisher Attribution

Foppert, A., K. A. Donohue, D. Randolph Watts, and K. L. Tracey (2017), Eddy heat flux across the Antarctic Circumpolar Current estimated from sea surface height standard deviation, *J. Geophys. Res. Oceans*, 122, 6947–6964, doi:10.1002/2017JC012837.
Available at: http://dx.doi.org/10.1002/2017JC012837

JOURNAL OF GEOPHYSICAL RESEARCH, VOL. ???, XXXX, DOI:10.1002/,

Eddy heat flux across the Antarctic Circumpolar Current estimated from sea surface height standard deviation

Annie Foppert,[1] Kathleen A. Donohue,[1] D. Randolph Watts,[1] Karen L. Tracey,[1]

[1]Graduate School of Oceanography, University of Rhode Island, Narragansett, RI, USA.

Key Points.

- SSH standard deviation, a proxy for eddy heat flux, characterizes and quantifies the spatial structure of EHF in the ACC
- EHF converges throughout the ACC: 1.06 PW enters from the north and 0.02 PW exits to the south
- Significant strengthening downgradient fluxes are seen at three of eight EHF hot spots between 1993 and 2014

Abstract.

Eddy heat flux (EHF) is a predominant mechanism for heat transport across the zonally unbounded mean flow of the Antarctic Circumpolar Current (ACC). Observations of dynamically relevant, divergent, four-year mean EHF in Drake Passage from the cDrake project, as well as previous studies of atmospheric and oceanic storm tracks, motivates the use of sea surface height (SSH) standard deviation, H^*, as a proxy for depth-integrated, downgradient, time-mean EHF ($[\overline{EHF}]$) in the ACC. Statistics from the Southern Ocean State Estimate corroborate this choice and validate throughout the ACC the spatial agreement between H^* and $[\overline{EHF}]$ seen locally in Drake Passage. Eight regions of elevated $[\overline{EHF}]$ are identified from nearly 23.5 years of satellite altimetry data. Elevated cross-front exchange usually does not span the full latitudinal width of the ACC in each region, implying a hand-off of heat between ACC fronts and frontal zones as they encounter the different $[\overline{EHF}]$ hot spots along their circumpolar path. Integrated along circumpolar streamlines, defined by mean SSH contours, there is a convergence of $\oint[\overline{EHF}]$ in the ACC: 1.06 PW enters from the north and 0.02 PW exits to the south.

Temporal trends in low-frequency [EHF] are calculated in a running-mean sense using H^* from overlapping 4-year subsets of SSH. Significant increases in downgradient [EHF] magnitude have occurred since 1993 at Kerguelen Plateau, Southeast Indian Ridge, and the Brazil-Malvinas Confluence, whereas the other five [$\overline{EHF}$] hot spots have insignificant trends of varying sign.

1. Introduction

Oceanic and atmospheric circulations transport heat poleward to balance the excess radiative heat experienced at the equator. In the southern hemisphere, the nearly zonal geostrophic flow of the Antarctic Circumpolar Current (ACC) acts as a barrier to direct poleward heat transport by the mean flow towards Antarctica and the southern seas. *de Szoeke and Levine* [1981] propose eddy heat flux (EHF) across the ACC as the main mechanism for balancing the northward ageostrophic Ekman flux and air-sea flux of heat out of the Southern Ocean, thus balancing the heat budget. Satellite altimetry and model studies reveal the eddy field of the ACC to be patchy, with hot spots of eddy activity found in the lee of major bathymetric features [e.g. *Thompson and Sallée*, 2012]. Understanding and quantifying EHF across the ACC, its relative contribution to the total heat flux across the ACC, and how it might be changing over time are essential for modeling and predicting how the Southern Ocean may modulate our future global climate.

Observations of the ACC are challenging to acquire and the lack thereof limits our ability to accurately quantify the relative contributions of eddy and mean heat flux to the total across the ACC. A mean heat flux due to the non-equivalent barotropic component of the mean velocity is small at any given point in the ACC, but an accumulation of these immeasurably small fluxes over a large area can lead to a significant, non-negligible heat flux across mean streamlines in a numerical model simulation [*Peña-Molino et al.*, 2014]. Quantifying the mean heat flux with observations is particularly difficult due to the large area and the high resolution and accuracy of velocity and temperature measurements required for a meaningful estimate of the flux. The variability of EHF in the ACC in both time and space, with episodic pulses of EHF occurring on timescales of several days [*Watts et al.*, 2016] and with localized regions of eddy activity [*Thompson and Sallée*, 2012], makes quantifying the total circumpolar integral of EHF through observations also a daunting task. Direct measurements of EHF in the ACC are limited to a handful of studies [*Watts et al.*, 2016; *Ferrari et al.*, 2014; *Sekma et al.*, 2013; *Phillips and Rintoul*, 2000], and the non-uniformity of the ACC eddy field complicates extrapolation from point measurements. Until the ACC and its eddy field are properly resolved with observations and the air-sea flux of heat is better constrained, closing the Southern Ocean heat budget will remain a matter of proxy measurements and bulk formula estimates. In this study, we use a high resolution numerical model and existing satellite altimetry to quantify EHF throughout the ACC.

Watts et al. [2016] demonstrate with direct observations in Drake Passage that baroclinic instability is the driving mechanism for large EHF events. These events release mean available potential energy (APE) from the system, reduce the slope of isopycnal surfaces by transporting heat down the mean temperature gradient, and produce eddy potential energy (EPE) [*Pedlosky*, 1987]. The simplest theory of baroclinic instability has meanders growing into eddies over time, yet spatial growth of eddies is also possible. In the ACC, meanders are forced by the local bathymetric configuration and mean flow, supporting the link between large bathymetric features and localized hot spots of eddy activity, that are sometimes referred to as oceanic storm tracks.

Sea surface height (SSH) data are readily available throughout the ACC from satellite altimetry, and we use the temporal standard deviation of SSH, H^*, as a proxy for time-mean EHF. *Holloway* [1986] uses SSH height variability, scaled by gravity and a local

Coriolis parameter, as a proxy for eddy diffusivity and estimates EHF via the mean temperature gradient. *Kushner and Held* [1998] apply that method analogously to two pressure levels in the atmosphere to reproduce maps of the divergent component of the EHF with some success. Furthermore, as the dynamics in the zonally unbounded ACC are similar to those in the atmosphere, albeit with different scales, those authors suggest a straightforward extension to oceanic storm tracks. This method of estimating eddy diffusivity has been applied to SSH variability in the Southern Ocean [e.g. *Keffer and Holloway*, 1988; *Karsten and Marshall*, 2002]. *Marshall et al.* [2006] and *Ferrari and Nikurashin* [2010] use other techniques for estimating eddy diffusivity from altimetric data, but again rely on a diffusive closure scheme to draw conclusions about eddy mixing. In this study, instead of seeking an eddy diffusivity or mixing coefficient to predict a downgradient flux, we use H^* directly as a proxy for the depth-integrated, divergent EHF in the ACC.

The eddy field of the ACC is likely to respond to the observed increase in circumpolar wind stress over the Southern Ocean [*Marshall*, 2003]. While direct observations are ideal for studying the ACC's response to the increasing winds, a large scale monitoring system is not yet in place and would be costly to implement. A proxy estimate of low-frequency, running-mean EHF via satellite H^* allows for investigation of trends in the circumpolar eddy field from January 1993 through December 2014. *Hogg et al.* [2014] diagnose the eddy kinetic energy (EKE) field in several sectors of the ACC and find variable trends over the 20 years of satellite data. However, recent model simulations by *Treguier et al.* [2010] have shown that trends in EKE do not necessarily reflect trends in EHF, and therefore EKE may not be the best metric for studying changes in the EHF field. Moreover, *Ferrari* *and Nikurashin* [2010] find, through estimating eddy diffusivity, suppressed mixing in the core of the ACC where there is enhanced EKE, again suggesting that EKE is not the best metric for EHF.

The following section presents motivating observations from the cDrake project [*Chereskin et al.*, 2012] in Drake Passage: elevated EHF and H^* are concentrated immediately downstream of the major bathymetric ridge, while the peak in mean surface EKE is offset further downstream (Section 2.1). This local relationship is confirmed throughout the circumpolar band of the ACC and a statistical relationship between EHF and H^* is developed using data from an eddy-permitting numerical model (Section 2.2). A power-law fit is applied to about 23.5 years of satellite data (Section 2.3). Circumpolar path-integrated values of EHF, its spatial pattern throughout the ACC, and long-term temporal trends in EHF at several "hot spots" are presented in Section 3. Section 4 provides a discussion of H^* as a proxy for EHF in the context of oceanic storm tracks, a comparison with the few other observations of EHF in the ACC, plus a discussion of the along- and cross-ACC structure of EHF and long-term trends. Section 5 summarizes the study.

2. Relating EHF to SSH variability

2.1. Observations in Drake Passage

An array of bottom-moored current- and pressure-recording inverted echo sounders (CPIES) was deployed in Drake Passage from November 2007 to November 2011 as part of the cDrake project (Figure 1a). Time series of hourly acoustic travel-time records measured by the IES and hourly near-bottom velocities measured by the current meter 50 m above the seafloor are three-day low-pass filtered and resampled every 12 hours, resulting in four-year records of τ and $\boldsymbol{u}_{ref}$, respectively, at each CPIES site. (The bold text indicates a horizontal vector quantity.) *Tracey et al.* [2013] describes the data collection and processing procedures in detail. A gravest empirical mode analysis based on regional hydrography provides a profile of temperature for every value of τ [*Chidichimo et al.*, 2014]. The near-bottom $\boldsymbol{u}_{ref}$ is assumed to be geostrophic and depth-independent, such that the total geostrophic velocity is the sum of the bottom-referenced baroclinic velocity profile and the reference velocity: $\boldsymbol{u}_{tot}(x, y, z, t) = \boldsymbol{u}_{bcb}(x, y, z, t) + \boldsymbol{u}_{ref}(x, y, t)$. A local dynamics array of CPIES was placed in the interfrontal zone between the mean position of the Subantarctic Front (SAF) and Polar Front (PF) in Drake Passage in a region of elevated eddy activity downstream of the Shackleton Fracture Zone (SFZ; Figure 1). The design of the local dynamics array, with 40 km spacing between sites, allows for three-dimensional optimal-interpolation mapping of twice-daily total geostrophic velocity and temperature fields [*Firing et al.*, 2014].

The dynamic importance lies in the divergent component of EHF, whereas the rotational component of EHF that circulates around contours of mean temperature variance is irrelevant dynamically [*Marshall and Shutts*, 1981]. That is, only the divergent EHF influences the dynamics of eddy-mean flow interactions. Measurements by CPIES naturally separate the large purely rotational EHF ($\boldsymbol{u}'_{bcb}T'$) from the $\boldsymbol{u}'_{ref}T'$, such that the latter contains all the divergent EHF, albeit with the possibility of a small residual rotational component [*Bishop et al.*, 2013; *Watts et al.*, 2016]. The prime denotes any deviation from the time mean, e.g. $T'(x, y, z, t) = T(x, y, z, t) - \bar{T}(x, y, z)$, where the overbar denotes the time-mean value. Time-mean, depth-integrated EHF is calculated, as in *Watts et al.* [2016], as:

$$[\overline{\boldsymbol{EHF}}] = \rho c_p \int_z \overline{\boldsymbol{u}'_{ref} \cdot T'} dz, \tag{1}$$

where square brackets denote a depth-integrated value and again the bold text indicates a horizontal vector quantity. Multiplication by a nominal density ($\rho = 1035$ kg m^{-3}) and specific heat of seawater ($c_p = 4000$ J kg^{-1} °C^{-1}) expresses the units as a proper heat flux.

Figure 1b shows $[\overline{\boldsymbol{EHF}}]_{cDrake}$, where the subscript denotes the dataset. Here, the vertical integration is from the surface to a common depth of 3500 m. We limit our analysis to the time-mean, depth-integrated $[\overline{\boldsymbol{EHF}}]_{cDrake}$ and present the results in units of MW m^{-1}. More details on EHF calculated from the cDrake CPIES, including the vertical structure and time series, can be found in *Watts et al.* [2016].

Figure 2 reinforces the claim made above, i.e. that $\boldsymbol{u}'_{bcb}T'$ is purely rotational and that $\boldsymbol{u}'_{ref}T'$ contains all of the divergence with a small rotational component remaining. The curl and the divergence of the total EHF ($\rho c_p \overline{\boldsymbol{u}'_{tot}T'}$) is compared with that of the baroclinic EHF ($\rho c_p \overline{\boldsymbol{u}'_{bcb}T'}$) and reference EHF ($\rho c_p \overline{\boldsymbol{u}'_{ref}T'}$). Here, for simplicity, the fluxes have been calculated at 400 m depth rather than depth-integrated, but the result is consistent. Figure 2 shows that, within the scatter due to mapping error, the divergence of the total $\overline{\boldsymbol{EHF}}$ is completely contained in the reference $\overline{\boldsymbol{EHF}}$. Likewise, the curl of the total $\overline{\boldsymbol{EHF}}$ is dominated by the curl of the baroclinic $\overline{\boldsymbol{EHF}}$. We also note that *Firing et al.* [2014] found good agreement between the mooring-based and CPIES-based velocities (R^2 between 0.67 and 0.85 in the upper 1000 m), temperatures (R^2 between 0.85 and 0.9), and *Watts et al.* [2016] found good agreement for the same comparison of velocity-temperature covariances (R^2 between 0.72 and 0.89). We are thus confident that the method for calculating the $[\overline{EHF}]$ using the near-bottom reference velocities in

Equation 1 greatly reduces the amount of rotational flux while retaining the divergent flux.

CPIES measurements also allow for calculation of total SSH, SSH_{cDrake}, as the sum of a reference SSH from directly-measured bottom pressure and bottom-referenced baroclinic SSH, as described by *Donohue et al.* [2016]. Figure 1c shows the standard deviation of the twice-daily SSH_{cDrake}, H^*_{cDrake} calculated with the CPIES data as:

$$H^* = \sqrt{\frac{1}{N-1}\sum_{i=1}^{N}(SSH_i - \overline{SSH})^2}, \tag{2}$$

where the subscript i represents the time index, and the overbar again denotes the time-mean value. We find that H^*_{cDrake} has a similar spatial pattern to $[\overline{\boldsymbol{EHF}}]_{cDrake}$: elevated values occur along the western edge of the local dynamics array immediately downstream of the SFZ (Figure 1b,c). While the spatial pattern of $[\overline{\boldsymbol{EHF}}]_{cDrake}$ has some interannual variability, depending on time period of averaging, the maximum $[\overline{\boldsymbol{EHF}}]_{cDrake}$ for any multiyear subset of the data is consistently on the western side of the CPIES array (see Figure 6 in *Watts et al.* [2016]). Moreover, the general agreement with the pattern of H^*_{cDrake} is also consistent for any multiyear subset of four-year record (not shown).

Figure 1d shows the mean surface EKE calculated from the cDrake CPIES data, $\overline{EKE}_{cDrake}$, as:

$$\overline{EKE} = \frac{1}{2}(\overline{u'^2 + v'^2}), \tag{3}$$

where $(u, v) = (u_{tot}, v_{tot})$ are the zonal and meridional geostrophic velocities at the sea surface. There are two peaks in $\overline{EKE}_{cDrake}$, with the highest value in the central longitudes of the local dynamics array, farther east than the peaks in $[\overline{\boldsymbol{EHF}}]_{cDrake}$ and H^*_{cDrake} (Figure 1b,c,d). Again, interannual variability in the spatial pattern of $\overline{EKE}_{cDrake}$ exists, but does not change its misalignment with $[\overline{\boldsymbol{EHF}}]_{cDrake}$ averaged over the same multiyear subset (not shown).

In Drake Passage, $[\overline{\boldsymbol{EHF}}]_{cDrake}$ and H^*_{cDrake} are concentrated in a relatively broad region immediately downstream of the SFZ, whereas $\overline{EKE}_{cDrake}$ exhibits smaller spatial scales. The peaks are separated by 1–2° of longitude. These observed spatial patterns from the cDrake project motivate our use of H^* as a proxy for $[\overline{\boldsymbol{EHF}}]$ throughout the entire ACC.

2.2. Circumpolar validation around the ACC

The Southern Ocean State Estimate (SOSE) validates that the spatial relationship between H^*_{cDrake} and $[\overline{\boldsymbol{EHF}}]_{cDrake}$ observed in Drake Pasage holds for the entire ACC (Figure 3). SOSE is an eddy-permitting general circulation model based on the MITgcm for all longitudes and latitudes south of 25°S [*Mazloff et al.*, 2010]. At 1/6° horizontal resolution and with 42 vertical levels, SOSE uses an iterative adjoint method to match the model's ocean state estimate to a suite of observational data sources — Argo floats, CPIES, satellite altimetry, etc — without introducing non-physical nudging terms into the equations of motion. Partial cells, rather than step functions, represent sloping bathymetry and give SOSE a better chance at capturing realistic near-bottom dynamics, making it well suited for this study. Several studies have shown that SOSE is an apt model for the investigation of ACC dynamics: *Peña-Molino et al.* [2014] examined the along- and across-stream components of the total geostrophic velocity and their respective mean heat fluxes, *Masich et al.* [2015] investigated topographic form stress, and *Abernathey et al.* [2016] considered water-mass transformation in the upper branch of the overturning circulation. We employ the most up-to-date output, Iteration 100, that contains six years of data from January

1, 2005 to December 31, 2010. Daily sea surface height, $SSH_{SOSE}(x, y, t)$, is available online (http://sose.uscd.edu) and its standard deviation, H^*_{SOSE}, given by Equation 2, is shown in Figure 3a.

The EHF calculation using SOSE output is analogous to the CPIES methodology to retain all of the dynamically-relevant divergent component of the flux (albeit with the possibility of a small residual rotational flux). Daily hydrostatic pressure potential anomaly and temperature throughout the water column were obtained directly from M. Mazloff (personal communication, March 2016). Geostrophic velocity is calculated at every point in SOSE from the surrounding pressure potential anomalies, avoiding partial cells. Reference velocities, $\boldsymbol{u}_{SOSE}(x, y, t)$, are the deepest of these geostrophic velocities at every location in the SOSE grid and are considered independent of depth, i.e. constant throughout the water column. The mean (median) height above the bottom of $\boldsymbol{u}_{SOSE}$ is 550 m (375 m) and the largest differences are found along steep sloping topography (not shown); the deepest layers of the model are 250 m thick.

Time-mean, depth-integrated $[\overline{\boldsymbol{EHF}}]_{SOSE}$ is then calculated with Equation 1, using SOSE reference velocity and temperature anomalies and the same nominal seawater density and specific heat as before (Figure 3b). An integration depth of 2046 m was chosen to capture the majority of the signal and for consistent calculations throughout the ACC. Only locations within the circumpolar band of mean streamlines ($\overline{SSH}_{SOSE} = -0.8$ to 0.2 m) and where the reference depth is as deep as or deeper than the integration depth are considered in the subsequent analysis. Finally, the horizontal flux vectors are projected across $\overline{SSH}_{SOSE}$ contours within the ACC band to give cross-frontal $[\overline{EHF}]_{SOSE}$

as a scalar quantity, such that the negative values in Figure 3b indicate downgradient fluxes (i.e. towards the southern seas and Antarctica).

In linear instability theory [*Pedlosky*, 1987], baroclinic instability acts to transport heat down the mean temperature gradient (or $\nabla\overline{SSH}$), yet about 20% of the $[\overline{EHF}]_{SOSE}$ values are up the mean gradient of $\overline{SSH}_{SOSE}$ (Figure 4a). In general, these upgradient values have smaller magnitudes and are associated with lower values of H^*_{SOSE} than the downgradient $[\overline{EHF}]_{SOSE}$ values. Figure 4b shows that, when averaged within 2.5×10^{-3} m wide H^*_{SOSE} bins and excluding bins with less than 30 points, the magnitudes of positive values of $[\overline{EHF}]_{SOSE}$ are significantly smaller than those that are negative, especially as H^*_{SOSE} increases. We investigated whether the small upgradient $[\overline{EHF}]_{SOSE}$ occurred near or south of the Polar Front, where the existence of a subsurface temperature inversion might cause eddy buoyancy fluxes to differ systematically in sign from heat fluxes. We found no preferred distribution for the relatively weak upgradient $[\overline{EHF}]_{SOSE}$. The sum of all downgradient $[\overline{EHF}]_{SOSE}$ points is an order of magnitude greater than the sum of upgradient points. For the rest of this study, we only consider downgradient fluxes.

There is a spatial alignment between downgradient $[\overline{EHF}]_{SOSE}$ and H^*_{SOSE} in the ACC: regions of elevated H^*_{SOSE} align with regions of elevated $[\overline{EHF}]_{SOSE}$ (Figure 3). A statistically significant power law exists between downgradient $[\overline{EHF}]_{SOSE}$ and H^*_{SOSE}, i.e. the variables are linearly related in log-log space (Figure 4b,c). The distribution is skewed such that there are many more points with low values of H^*_{SOSE} and $[\overline{EHF}]_{SOSE}$ (Figure 4a), as expected from the handful of regions with elevated values of $[\overline{EHF}]_{SOSE}$ and H^*_{SOSE} in Figure 3. For example, within 2.5×10^{-3} m wide H^*_{SOSE} bins, there are 60 times more points of downgradient $[\overline{EHF}]_{SOSE}$ with H^*_{SOSE} between 0.1 m and 0.15 m than there are with H^*_{SOSE} between 0.2 m and 0.25 m (Figure 4a). To avoid biasing the fit with lower values of H^*_{SOSE}, $[\overline{EHF}]_{SOSE}$ values are averaged within H^*_{SOSE} bins prior to calculating the power-law fit (Figure 4b,c). Outliers, shown as light gray points in Figure 4c, are excluded by only using $[\overline{EHF}]_{SOSE}$ values found between the 5th and 95th percentile in each bin and by excluding H^*_{SOSE} bins that have fewer than 30 points. The bin-averaged power law is

$$[\overline{EHF}] = A \cdot {H^*}^B, \tag{4}$$

where $[\overline{EHF}] = [\overline{EHF}]_{SOSE-fit}$ is the scalar quantity of downgradient, depth-integrated flux in units of MW m^{-1} and $H^* = H^*_{SOSE}$ is in meters. The best-fit coefficients, $A = -(1.85 \pm 0.17) \times 10^4$ and $B = 3.95 \pm 0.12$, give a bin-averaged R^2 value of 0.93. The negative value of A guarantees downgradient values everywhere. In log-log space, B is the slope of the line and $|A| = 10^\alpha$, where α is the y-intercept.

The observed $[\overline{EHF}]_{cDrake}$ values (described in Section 2.1) fall within the scatter of the circumpolar SOSE values (Figure 4c, red squares). Here, we present $[\overline{EHF}]_{cDrake}$ values that have been projected across the mean satellite SSH field (described in Section 2.3) averaged over the four years of the cDrake experiment. The data are from all CPIES sites with downgradient values of $[\overline{EHF}]_{cDrake}$, including those along the full-passage transect shown in Figure 1a. Additionally, the vertical integration is from the surface to 2000 m, rather than to 3500 m as in Figure 1b, for an appropriate comparison with $[\overline{EHF}]_{SOSE}$. On average, surface-to-3500 m integral values of $[\overline{EHF}]_{cDrake}$ are 1.3 times greater than surface-to-2000 m integral values.

A noticeable feature of Figure 4c is the apparent truncation of H^*_{SOSE} near 0.09 m, whereas H^*_{cDrake} and other observations extend to lower values. The lowest value observed at the southern CPIES sites ($H^*_{cDrake} = 0.0697$ m) is about 80% of the lowest value of H^*_{SOSE} (= 0.0875 m). This elevated floor of H^*_{SOSE} is mainly due to high frequency, rapidly propagating waves within the model, but not in the cDrake observations (not shown). Arguably, the dynamics in SOSE capture the baroclinic instability process driving the $[\overline{EHF}]_{SOSE}$ signal with or without the presence of these high frequency waves. Moreover, low-pass filtering the SSH_{SOSE} data does not improve the power-law fit in terms of mean square error or R^2 value, so H^*_{SOSE} is calculated from the unfiltered daily SSH_{SOSE} fields. Additionally, the higher values of H^*_{SOSE} have similar magnitudes as H^*_{cDrake}, and it is in these regions of greatest SSH variability where the strongest $[\overline{EHF}]$ occurs.

Comparison of $[\overline{EHF}]$ calculated directly in SOSE with that estimated from H^*_{SOSE} using Equation 4 provides further confidence in the H^* proxy. Integrated along circumpolar contours of $\overline{SSH}_{SOSE}$, the estimated $\oint[\overline{EHF}]_{SOSE-fit}$ values agree well with the directly calculated $\oint[\overline{EHF}]_{SOSE}$ values, where $\oint(\cdot)$ denotes a circumpolar path-integrated value (Figure 5a). For orientation within the ACC mean flow field, the mean geostrophic speed in the uppermost vertical layer (5 m depth) along each $\overline{SSH}_{SOSE}$ contour is shown in Figure 5b. A nominal streamline for the SAF is $\overline{SSH}_{SOSE} = 0.0$ m contour, with along-stream speeds of about 0.2 m s^{-1}. The estimated $\oint[\overline{EHF}]_{SOSE-fit}$ is slightly weaker than its directly calculated counterpart across some streamlines and slightly stronger across others, with a root-mean-square difference of 0.02 PW (Figure 5a). The largest differences between path-integrated values are near the SAF, where the magnitude of $\oint[\overline{EHF}]_{SOSE-fit}$ is 0.06 PW stronger than that of $\oint[\overline{EHF}]_{SOSE}$ and remains less than 10% of the mean absolute value of -0.7 PW. Both $\oint[\overline{EHF}]_{SOSE}$ and $\oint[\overline{EHF}]_{SOSE-fit}$ are weakest along the southern edge of the ACC where the path-integrated heat flux is about -0.2 PW. The magnitudes of $\oint[\overline{EHF}]_{SOSE-fit}$ and $\oint[\overline{EHF}]_{SOSE}$ increase by more than a factor of 3 as $\overline{SSH}_{SOSE}$ increases across the southern and central streamlines, and decrease slightly on the northern flank of the ACC (north of the SAF). This pattern of $\oint[\overline{EHF}]$ is indicative of a convergence of heat in streamlines south of the SAF and a divergence north of the SAF.

2.3. Application to satellite data

The power-law fit given by Equation 4 is now applied to satellite SSH data to estimate time-mean, depth-integrated EHF, $[\overline{EHF}]_{sat}$, in the ACC. Again, the direction of the flux is treated as downgradient (as ensured by the negative coefficient in Equation 4). Here, $SSH_{sat}(x, y, t)$ is the addition of the CNES-CLS13 mean dynamic topography to the Ssalto/Duacs gridded daily mean sea level anomaly (with a consistent reference period from 1993-2012). The mean dynamic topography was produced by CLS Space Oceanography Division and the sea level anomalies are produced and distributed by the Copernicus Marine and Environment Monitoring Service (as of May 2015); both are available online through AVISO at http://www.aviso.altimetry.fr. For this study, we use the two-satellite 'ref' product of mean sea level anomaly to additionally investigate long-term temporal trends in the record. The resulting SSH_{sat} record is almost 23.5 years of data from January 1993 to May 2016 at 1/4° horizontal resolution.

This analysis uses the SSH_{sat} field to calculate several variables: H^*_{sat}, $[\overline{EHF}]_{sat}$, $\oint[\overline{EHF}]_{sat}$, $[EHF_{sat}]$, and surface $\overline{EKE}_{sat}$. Standard deviation, H^*_{sat}, is calculated by applying Equation 2 to the full-length SSH_{sat} record. For consistency with analysis in

SOSE, the power law is only applied to points within the circumpolar ACC band, defined as $\overline{SSH}_{sat} = -1.0$ to 0.3 m. The circumpolar band is chosen such that the $\overline{SSH}_{sat}$ contours are continuous throughout the Southern Ocean and pass through Drake Passage. Downgradient $[\overline{EHF}]_{sat}$ is estimated throughout the ACC from the H^*_{sat} field using the power law (Equation 4). $[\overline{EHF}]_{sat}$ and its path-integrated counterpart, $\oint[\overline{EHF}]_{sat}$, represent the nearly 23.5-year mean divergent eddy flux of heat, depth-integrated to 2000 m, and directed across mean $\overline{SSH}_{sat}$ contours towards Antarctica and the southern seas. Additionally, time series of low-frequency, running-mean $[EHF]_{sat}$ is estimated with the same equation, using a time series of H^*_{sat} calculated from 4-year subsets of SSH_{sat} overlapped by 2 years from 1993 through 2014. Finally, $\overline{EKE}_{sat}$ is calculated with Equation 3 using SSH_{sat}-derived geostrophic velocities, and is discussed in a few regions of elevated eddy activity in the context of oceanic storm tracks (Section 4.1).

3. Cross-ACC eddy heat flux

3.1. Circumpolar path-integrated $\oint[\overline{EHF}]_{sat}$

Integrated along circumpolar contours of $\overline{SSH}_{sat}$, the maximum magnitude of downgradient $\oint[\overline{EHF}]_{sat}$ of 1.06 PW occurs on the northern edge of the ACC (Figure 6a). Figure 6b shows the mean surface geostrophic speed, calculated from the $\overline{SSH}_{sat}$ fields, as well as labels for nominal ACC fronts determined from the mean along-stream surface geostrophic speed ($\overline{SSH}_{sat}$ of SAF=-0.1 m; PF=-0.4 m; SACCF =-0.7 m). The overall pattern of decreasing $\oint[\overline{EHF}]_{sat}$ magnitude with decreasing $\overline{SSH}_{sat}$ indicates a lateral convergence of heat due to eddies into the ACC (Figure 6a). The steeper slope on the northern side of the SAF, compared to the nearly constant slope south of the SAF, represents a stronger convergence of $\oint[\overline{EHF}]_{sat}$ in the northern flank of the ACC.

An uncertainty in $\oint[\overline{EHF}]_{sat}$ of 0.02 PW is taken as the root-mean-square difference between $\oint[\overline{EHF}]_{SOSE}$ and $\oint[\overline{EHF}]_{SOSE-fit}$ (Figure 5a). For simplicity, this uncertainty is assumed to be independent of the circumpolar path of integration, i.e. independent of $\overline{SSH}_{sat}$ contour. Therefore, the $\oint[\overline{EHF}]_{sat}$ values on the southern edge of the ACC are statistically indistinguishable from zero (Figure 6a). Point-wise uncertainties in the $[\overline{EHF}]_{sat}$ estimates are not discussed, as most interest lies in the qualitative spatial distribution and quantitative circumpolar integrations. However, it can be noted that the rms difference between the bin-mean values of $[\overline{EHF}]_{SOSE}$ and the power-law fit is 10.5 MW m^{-1} (Figure 4b).

3.2. Spatial distribution of $[\overline{EHF}]_{sat}$

There are eight regions of relatively large values, i.e. hot spots, of $[\overline{EHF}]_{sat}$ around the ACC, shown by the red colored dots in Figure 7a. We define these hot spots as broad regions where $[\overline{EHF}]_{sat} \leq -10$ MW m^{-1} (approximately equivalent to $H^*_{sat} \geq$ 0.15 m), more than double the ACC average of -5.1 MW m^{-1}. Six of these regions are associated with interactions between the ACC and major bathymetric features and two regions are associated with interactions with western boundary currents of subtropical gyres. Eastward from 0°E, the hot spots associated with major bathymetric features occur at the Southwest Indian Ridge (SWIR; 20–40°E), Kerguelen Plateau (KP; 81–96°E), Southeast Indian Ridge (SEIR; 115–160°E), Maquarie Ridge (MR; 160–180°E), Pacific Antarctic Rise (PAR; 205–230°E), and Drake Passage (DP; 285–315°E, south of 52°S); the hot spots associated with western boundary currents are the Agulhas Return Current (ARC; 10–83.5°E, northern flank of ACC) and the Brazil-Malvinas Confluence (BMC; 300–335°E, north of DP where they overlap longitudes). The longitudinal limits of the $[\overline{EHF}]_{sat}$ hot spots are denoted by horizontal bars in Figure 7b; latitudinal limits only exist for regions that overlap in longitude. It can be noted that there is little interaction between the ACC and the Eastern Australian Current, the western boundary current of the subtropical South Pacific gyre, as the circumpolar band of $\overline{SSH}_{sat}$ excludes almost all of it from this study. Here, DP spans the Phoenix Antarctic Ridge, the Shackleton Fracture Zone, and the Scotia Arc (including Shag Rocks); the BMC region includes the entire Zappiola Anticyclone; MR region also includes the area south of Campbell Plateau; and the PAR includes both the Udintsev and Eltanin Fracture Zones.

Along circumpolar streamlines, the relative contribution of each hot spot to the total $\oint[\overline{EHF}]_{sat}$ varies (Table 1; Figure 7). Few regions of elevated $[\overline{EHF}]_{sat}$ influence all ACC streamlines. The main pulses of $[\overline{EHF}]_{sat}$ along the northern edge of the ACC are strongly tied to its interactions with the subtropical western boundary currents. That is, 89% of the total $\oint[\overline{EHF}]_{sat}$ crosses the $\overline{SSH}_{sat} = 0.3$ m contour at the ARC and BMC. It is not surprising that the ARC and BMC become increasingly less influential for more southern ACC streamlines. Across the SAF ($\overline{SSH}_{sat} = -0.1$ m), the two western boundary currents account for less than half (41%) of the total $\oint[\overline{EHF}]_{sat}$, and more occurs at the SAF's interaction with the SEIR (16%) than the ARC. $\oint[\overline{EHF}]_{sat}$ across a nominal PF ($\overline{SSH}_{sat} = -0.4$ m) accumulates from its interaction with all eight hot spots, with DP accounting for nearly a quarter of the total (23%). The SWIR and KP play a more prominent role in the $\oint[\overline{EHF}]_{sat}$ across the more southern streamlines of the ACC, with each accounting for between 21 and 26% of the total crossing the SACCF ($\overline{SSH}_{sat} = -0.8$ m) and exiting the southern edge of the ACC ($\overline{SSH}_{sat} = -1.0$ m). That different streamlines have different hot spots of $[\overline{EHF}]_{sat}$ suggests there is a hand-off of heat from one front or frontal zone to another along the circumpolar path of the ACC.

The DP and BMC regions require a more detailed view, as the northern streamlines of the ACC turn sharply northward upon exiting the east side of DP before meeting the southward flowing Brazil Current and turning eastward again. Figure 7c shows an expanded view of the cumulative $[\overline{EHF}]_{sat}$ as a percent of the total $\oint[\overline{EHF}]_{sat}$ along mean ACC streamlines in the DP and BMC regions as a function of along-stream distance (rather than as a function of longitude, as in Figure 7b). The contours are drawn from 360°E back to 275°E, i.e. ending at the black dots in Figure 7a, such that 0 km is equivalent to 360°E. The DP region is designated by a thin gray and white dashed line and the BMC region by the thin black line within the colored lines; 52°S divides the two regions where their longitudinal ranges overlap. As noted previously, interactions with subtropical western boundary currents, i.e. BMC, are predominant sources of $[\overline{EHF}]_{sat}$ along the northern streamlines of the ACC and become less influential for more southern streamlines. The PF and the SACCF have a greater percentage of their respective total $\oint[\overline{EHF}]_{sat}$ occurring in DP than compared to the BMC (see also Table 1). The total $\oint[\overline{EHF}]_{sat}$ exiting the southern edge of the ACC has a 11% contribution from the BMC region, at the southeastern edge of the Zappiola Anticyclone, but recall the total path-integrated value on this contour is not significantly different from zero.

A small fraction of the total $\oint[\overline{EHF}]_{sat}$ along each $\overline{SSH}_{sat}$ contour is produced within regions outside of the hot spots. At the northern edge, 95% of the total $\oint[\overline{EHF}]_{sat}$ occurs within the hot spots; thus a mere 5% occurs outside these eight regions (Table 1. In contrast, at the southern edge, 16% of the total $\oint[\overline{EHF}]_{sat}$ is produced in regions outside the $[\overline{EHF}]_{sat}$ hot spots.

3.3. Low-frequency $[EHF_{sat}]$ time series

There is much interest in how the ACC eddy field responds to changes in zonal wind stress associated with the increasing wind stress noted by *Marshall* [2003]. To investigate long-term trends in $[EHF]_{sat}$, each of the eight regions of enhanced fluxes is considered individually (boxes in Figure 8a). A time series of running-mean $[EHF]_{sat}$ and its linear trend are calculated at every point with enhanced $[\overline{EHF}]_{sat}$ ($\geq$ 10 MW m^{-1}; orange and red colors in Figure 8a). The time series and temporal trends are then averaged within each $[\overline{EHF}]_{sat}$ hot spot, resulting in eight regional-mean time series of low-frequency $[EHF]_{sat}$ and a respective trend (Figure 8b). Note that the trends are calculated using complete 4-year subsets of time and therefore only include data through the end of 2014. The trends are listed in the legend as a percentage of the regional-mean $[\overline{EHF}]_{sat}$ per year.

Figure 8b shows the low-frequency $[EHF]_{sat}$ anomaly time series for each hot spot. We include the most recent four years of data in the time series as an unfilled symbol connected by a dashed line to indicate that it was not used in the trend calculation, as it overlaps the preceding 4 year interval by more than 2 years (as labelled). The inter-annual variability in the time series makes the trends particularly dependent on the choice of endpoints for the linear regression, and only three of the $[\overline{EHF}]_{sat}$ hot spots have statistically significant trends: KP, SEIR, and BMC. Of these trends, KP has the highest R^2 value of 0.76, while SIER and BMC have R^2 values of 0.46 and 0.39, respectively. Additionally, there is a suggestion of a low-frequency signal with a period of 6–12 years in most of the records, especially that of the ARC (Figure 8b).

Regions without large trends are grouped in the upper panel and regions with large trends are grouped in the lower panel. (Here, large means the magnitude of the trend is greater than 0.25 MW m^{-1} yr^{-1} or greater than 1.0% of the regional mean per year.) Large negative trends in running-mean $[EHF]_{sat}$, i.e. increasing $[EHF]_{sat}$ magnitudes over time, are seen at KP, SEIR, and MR. These bathymetric features are found between 60°E and 180°E in the Indian sector and entering the Pacific sector of the ACC.

The SWIR experiences a large, but insignificant, decrease in $[EHF]_{sat}$ magnitude of −1.2% of the regional mean per year over the 22 years of SSH_{sat} data (Figure 8b). It can be noted that including the last 4 years of SSH_{sat} data, from May 2012 to May 2016, with an adjusted period of overlap, results in a decrease in magnitude of the trend at the SWIR but does not change its sign. That is, even with the most recent data, the magnitude of $[EHF]_{sat}$ at the SWIR is decreasing (i.e. there is a positive trend in Figure 8b). DP and ARC also exhibit decreases in $[EHF]_{sat}$ magnitude, albeit smaller than that at the SWIR.

4. Discussion

4.1. H^* as a proxy for $[\overline{EHF}]$

The spatial distribution of time-mean, depth-integrated, downgradient, divergent EHF in the ACC is patchy, with enhanced fluxes in the lee of major bathymetric features and in regions where the ACC interacts with western boundary currents of subtropical gyres. That there are eddy activity hot spots is not new [e.g *Thompson and Sallée*, 2012; *Thompson and Naveira-Garabato*, 2014]), but here the fluxes have been quantified by using satellite altimetry, specifically H^*_{sat}, as a proxy for $[\overline{EHF}]_{sat}$ using the power law in Equation 4.

Previous studies have used SSH variability, scaled by g/f, as a proxy for eddy diffusivity and have estimated EHF via the mean temperature gradient [e.g *Holloway*, 1986; *Keffer and Holloway*, 1988]. *Kushner and Held* [1998] successfully reproduce maps of the divergent component of the EHF by applying that method analogously to the atmosphere. Applied to the Southern Ocean, this method estimates about 0.5 PW of poleward EHF at 60°S [*Keffer and Holloway*, 1988]. *Karsten and Marshall* [2002] estimate surface diffusivities in the Southern Ocean directly from the scaled SSH variability, and a constant of proportionality. We find that scaling H^*_{SOSE} by g/f did not improve the statistics of the bin-averaged power law and choose to quantify depth-integrated, time-mean, divergent $[\overline{EHF}]_{sat}$ directly from H^*_{sat} (Equation 4). Moreover, we estimate $[\overline{EHF}]_{sat}$ directly from an empirical relationship with H^*_{sat} rather than through a diffusive closure argument, thus bypassing the need to estimate an eddy diffusivity.

Abernathey and Cessi [2014] show that cross-stream eddy diffusivity is directly related to the downgradient $[\overline{EHF}]$ and cross-stream $[\nabla\bar{T}]$. Even with the advent of Argo floats, maps of subsurface temperature gradient at high resolution are not readily available for this calculation. Moreover, the use of depth-integrated quantities erases any vertical structure in the diffusivity. It has been shown in SOSE that there is a subsurface eddy diffusivity maximum associated with 'steering levels' where the mean flow matches the eddy propagation speed [*Abernathey et al.*, 2010]. Therefore, we focus on $[\overline{EHF}]$ and simply note that, with some care taken in estimating $[\nabla\bar{T}]$, the spatial pattern of depth-integrated eddy diffusivity could later be quantified. Here, we can look at the qualitative pattern of path-integrated eddy diffusivity by assuming that $[\nabla\bar{T}]$ is proportional to the mean surface speed along each $\overline{SSH}_{sat}$ contour in Figure 6b. The patterns in Figure 6 imply larger eddy diffusivities north of the SAF and weaker diffusivities in the rest of the ACC. This qualitative result is in accordance with recent work showing eddy mixing suppression at the core of the ACC and enhanced mixing on the equatorward flank [e.g. *Marshall et al.*, 2006; *Ferrari and Nikurashin*, 2010].

Idealized model studies find that baroclinic conversion, and thus $\overline{EHF}$, occurs in the region of highest baroclinicity, and that there is a spatial offset between this region and the region of highest eddy activity and $\overline{EKE}$ [e.g. *Chang and Orlanski*, 1993; *Chapman et al.*, 2015]. Baroclinic instability converts mean APE to EPE through a flux of heat across the mean temperature (or $\overline{SSH}$) gradient [*Pedlosky*, 1987]. SSH_{cDrake} variance, i.e. H^{*2}_{cDrake}, is dominated by the bottom-referenced baroclinic (or buoyancy) term rather than the bottom pressure term (comparison of Figure 3d and 3e in *Donohue et al.* [2016]). Consequently, H^{*2}_{cDrake} corresponds mainly to the surface expression of $\overline{EPE}$ $(=\overline{b'b'}/\bar{b}_z$, where b is buoyancy). Therefore, enhanced H^{*}_{cDrake} immediately downstream of SFZ seen in Figure 1c is interpreted as the production of EPE through conversion from mean APE due to baroclinic instability. This suggests why H^* is observed to be a good indicator of $[\overline{EHF}]$, because of growth by baroclinic instability in the most unstable regions.

Contours of $[\overline{EHF}]_{cDrake}$ and H^{*}_{cDrake} generally trend north-south (roughly parallel to the bathymetry of the SFZ) and are enhanced immediately downstream of the SFZ, while peak values of $\overline{EKE}_{cDrake}$ are found farther downstream, i.e. farther east in the CPIES array (Figure 1). This is in accordance with work on oceanic storm tracks by *Chapman et al.* [2015]. Those authors show, using wave activity flux vectors calculated in a primitive equation model, that $\overline{EHF}$ (diagnosed as the vertical component of the wave activity vector) is highest directly downstream of an idealized ridge. In this region of enhanced baroclinic instability, meanders actively grow into eddies, EHF converts mean APE into EPE, and EKE is increasing in the along-stream direction. We posit that the growth and persistence of baroclinic eddies, in both time and space, results in a spatial offset between peaks of $[\overline{EHF}]$ (as well as $\overline{EPE}$ and H^*) and $\overline{EKE}$.

While baroclinic instability, $[\overline{EHF}]$, and $\overline{EPE}$ characteristically concentrate leading into the produced meander, the location of highest $\overline{EKE}$ is more variable. That is, the location where $\overline{EKE}$ is highest depends on additional factors (bathymetric configuration, eddy-mean flow interactions, etc.) that can advance or retard eddy growth downstream. Figure 9 provides observational evidence at additional locations of the spatial offset between H^*_{sat} (and thus $[\overline{EHF}]_{sat}$) and $\overline{EKE}_{sat}$ in oceanic storm tracks from a zoomed-in subsection of three $[\overline{EHF}]_{sat}$ hot spots: SWIR, SEIR, and MR. We present H^{*2}_{sat} (top row), rather than H^*_{sat}, as it is analogous to EPE and therefore a parallel quantity to $\overline{EKE}_{sat}$ (bottom row).

Figure 9 shows the offset between peaks of H^{*2}_{sat} and $\overline{EKE}_{sat}$ at the SWIR and MR to be less than one degree of longitude, or about 50–100 km. This is about the same as, or slightly shorter than, the offset observed in DP from the cDrake CPIES data (Figure 1). The SEIR region is a bit more complicated, with the suggestion of both a northern and southern storm track. Figure 9e shows peaks of $\overline{EKE}_{sat}$ (plotted here as $2\cdot\overline{EKE}_{sat}$ to use consistent limits for the colorbar) along both the $\overline{SSH}_{sat} = 0.2$ m and $\overline{SSH}_{sat} = -0.2$ m contours. Along the northern contour, there is a small peak in $\overline{EKE}_{sat}$ near 125°E and another elongated peak near 128°E that extends to 131°E. The offset between H^{*2}_{sat} and the first $\overline{EKE}_{sat}$ peak along this northern contour is similar to that seen in the other regions. The offset between H^{*2}_{sat} and the second $\overline{EKE}_{sat}$ peak along this contour is about 4° of longitude, closer to the suggested offset of about 350 km in the modeling work of *Chapman et al.* [2015]. The pattern of heightened H^{*2}_{sat} followed by heightened $\overline{EKE}_{sat}$ is not clear in all eight hot spots, but we note that the ACC is much more complicated than an idealized model and that we do not expect to see the characteristic pattern of storm tracks everywhere, especially in regions of complicated bathymetry. Nevertheless, in the three regions of enhanced $[\overline{EHF}]_{sat}$ in Figure 9, as well as in DP observations, the peaks in H^{*2} (or H^* and thus $[\overline{EHF}]$) generally occur where $\overline{EKE}$ is increasing in the along-stream direction.

4.2. Comparison with observations

Observations of EHF in the Southern Ocean are sparse, and contamination by the dynamically irrelevant rotational EHF can confound interpretation. A large rotational component can be removed from the full EHF in CPIES measurements by using the depth-independent, near-bottom, reference velocities (the technique used by *Watts et al.* [2016] and described in Section 2.1) or from current-meter data by projecting the data into a low-passed shear-coordinate system (used by *Sekma et al.* [2013], *Phillips and Rintoul* [2000], and *Ferrari et al.* [2014]). When significant depth-mean values are converted to surface-to-2000 m depth-integrated values, the latter two studies find downgradient $[\overline{EHF}]$ from south of Tasmania and Drake Passage (respectively) ranging from 17 to 26 MW m^{-1}. *Sekma et al.* [2013] find insignificant depth-mean downgradient values of EHF in the narrow constraints of Fawn Trough (with a depth-integrated equivalent of 1 MW m^{-1} or less, depending on the reference frame). The significant values are plotted in Figure 4c (gray and blue triangles) on a log-log scale as a function of H^*_{sat}, where the standard deviation is taken over the sampling period corresponding to the respective studies. These values, as well as those from cDrake (red squares), fall within the upper limits of the scatter of all ACC locations in SOSE (Figure 4c).

If the rotational component is accurately known at every grid point and well enough resolved, its contribution to the circumpolar path-integrated EHF is exactly zero, by definition. The spatial distribution of EHF along contours may still be contaminated by the rotational component, but the total path-integrated value is purely divergent. However, if the measurements are noisy or not well resolved around the circumpolar path, the path-integrated rotational EHF may produce a large false contribution. Our results of circumpolar path-integrated $[\overline{EHF}]_{sat}$ magnitude decreasing from about 1.06 PW to 0.02 PW in the upper 2000 m of the ACC agree well with the results of *Gille* [2003] from ALACE floats (0.9 PW decreasing to 0.3 PW across the ACC) and *Zhiwei et al.* [2014] from ARGO floats (0.38 PW in the ACC band of streamlines). It can be noted that the alternating poleward-equatorward EHF found in ARGO float data by *Zhiwei et al.* [2014] may be due to contamination of the signal locally by a large rotational component, and may not be dynamically relevant.

4.3. Across-stream structure of $\oint[\overline{\boldsymbol{EHF}}]_{sat}$

4.3.1. Implications for Southern Ocean heat budget

In a balanced world, the amount of heat crossing a streamline's vertical-circumpolar surface is equal to the total air-sea heat flux out of the sea surface encompassed south that closed streamline. In this case, the circumpolar and vertical integral of total heat flux across streamlines of $\overline{SSH}_{sat}$ must balance the air-sea flux of heat out of the ocean to its south (neglecting a nominal mean geothermal heating from the seafloor of less than 50 mW m^{-2} [*Adcroft et al.*, 2001]). Estimates of air-sea flux come with uncertainties of up to 70% [*Large and Nurser*, 2001], yet the general consensus between models [e.g. *Volkov et al.*, 2010; *Meijers et al.*, 2007] and bulk formulae estimates [*Large and Nurser*, 2001] is on the order of tenths of petawatts out of the Southern Ocean. Several recent studies have used 0.4 PW as a typical value [e.g. *Watts et al.*, 2016; *Sekma et al.*, 2013]. Historically, 60°S has been chosen as the latitude of integration because the ocean is unblocked by land at all longitudes there. However, around the globe the ACC spans a wide range of latitudes and it makes more sense conceptually to integrate along a circumpolar streamline instead.

The total heat flux across mean ACC streamlines is a combination of eddy and mean heat fluxes. While *de Szoeke and Levine* [1981] show that the mean heat flux is dominated by the ageostrophic Ekman heat flux ($\overline{EkHF}$), *Peña-Molino et al.* [2014] show that there is also a non-negligible contribution from the non-equivalent barotropic veering of the mean baroclinic velocity field ($\overline{nonEBHF}$). *Levitus* [1987] use monthly climatological wind and sea surface temperature to estimate global Ekman heat flux. Integrating along latitudes, those authors find $\overline{EkHF} = 0.38$ PW at 50.5°S (i.e. northward heat flux) that decreases to 0.00 PW at 61.5°S. More recently, *Abernathey and Cessi* [2014] calculate a northward $\overline{EkHF}$ to be 0.3 PW at the PF in SOSE, agreeing with the climatology-based estimate of *Levitus* [1987]. Additionally, *Peña-Molino et al.* [2014] show that the non-equivalent barotropic component of the mean geostrophic velocity contributes -0.2 PW entering the northern edge of the ACC and 0.0 PW exiting the southern edge, i.e. downgradient $\overline{nonEBHF}$. Thus, we consider the mean heat flux across the PF to be a combination of 0.3 PW of $\overline{EkHF}$ and -0.1 PW of $\overline{nonEBHF}$, to give a total of 0.2 PW in the northward/upgradient direction.

Our estimates of $\oint[\overline{EHF}]_{sat}$ find -0.24 ± 0.02 PW crossing the PF (Figure 6a; Table 1). When $\oint[\overline{EHF}]_{sat}$ is scaled up to "full-depth" ACC using the factor of 1.3 from the mean ratio of $[\overline{EHF}]_{cDrake}$ integrated from the surface to 3500 m to that integrated to 2000 m depth (see Section 2.2), we find -0.31 PW crosses PF (Figure 6a). Total heat flux across the PF, the combination of 0.2 PW (northward/upgradient) mean heat flux and -0.3 PW due to eddies, is -0.1 PW. Thus, ocean processes transport 0.1 PW across the PF towards Antarctica and the southern seas. The air-sea flux required to balance the total heat flux across the PF estimated here, i.e. an ocean loss of 0.1 PW to the atmosphere south of the PF, is well below the 0.4 PW cited above. We note that it falls just outside of the 70% uncertainty associated with the current estimate of air-sea flux. While the estimates given here have uncertainties of their own, as the sum of small terms where the sign seems well established, the uncertainties are less than the 0.3 PW difference from 0.4 PW of air-sea heat flux. We suggest that 0.4 PW is an overestimate of the air-sea heat flux south of the PF. Direct observations of the air-sea heat flux over the Southern Ocean are needed to better constrain the Southern Hemisphere heat budget, as its magnitude is estimated here as a residual.

4.3.2. Inferences from lateral heat convergence

The shape of $\oint[\overline{EHF}]_{sat}$ as a function of $\overline{SSH}_{sat}$ in Figure 6a implies a convergence of heat by eddies across all the streamlines of the ACC. On the southern edge of the ACC, $\oint[\overline{EHF}]_{sat}$ approaches zero. This is in agreement with the modeling work of *Volkov et al.* [2010] where path-integrated $\overline{EHF}$ is negligible south of 65°S. Interestingly, the shape of the $\oint[\overline{EHF}]$ curve north of the SAF where the flux is dominated by interactions with the subtropical western boundary currents differs greatly between SOSE and satellite data. Comparison of Figure 5a and 6a reveals an enhanced convergence of $\oint[\overline{EHF}]_{sat}$ north of the SAF that is not apparent in $\oint[\overline{EHF}]_{SOSE}$ or $\oint[\overline{EHF}]_{SOSE-fit}$. *Volkov et al.* [2010] also show enhanced latitudinally integrated $\overline{E}HF$ convergence around 60°S. SOSE, on the other hand, has a divergence of $\oint[\overline{EHF}]_{SOSE}$ and $\oint[\overline{EHF}]_{SOSE-fit}$ north of the SAF. Close inspection of H^*_{SOSE} and H^*_{sat} (via $[\overline{EHF}]_{sat}$) reveals a different pattern and magnitude of the SSH variability, especially at the BMC (Figure 3a and 7a). The complex bathymetry of the Argentine Basin, the Zappiola Anticyclone, and the exact location of the fronts have a large impact on the $[\overline{EHF}]$ in the region. Further observations and higher resolution modeling studies are needed to determine processes controlling the pattern and strength of $[\overline{EHF}]$, especially in this particular region.

The convergence of $\oint[\overline{EHF}]_{sat}$ throughout the ACC implies an along-stream temperature change at the $[\overline{EHF}]_{sat}$ hot spots. Assuming there are no sources or sinks of heat at mid-depth in the ACC and a steady-state long-term mean in stream-wise temperature, the temperature equation reduces to a balance between along-stream temperature advection and cross-stream (or downgradient) $\overline{EHF}$ convergence, i.e. $U(\partial T/\partial s) = -(\partial/\partial n)\overline{V'T'}$. Here, U and V are the down- and cross-stream components of the velocity at, say, 500 m depth. Note that in simplifying this equation, we assume divergence of along-stream $\overline{U'T'}$ is small and there is no mean cross-stream velocity. This can be rearranged to estimate the scale of downstream temperature changes, $\Delta T = -(\overline{EHF}/U)(L_s/L_n)$, where L_s and L_n are down- and cross-stream length scales. We use scales based on the observed mean structure of the PF and EHF in Drake Passage. The mean width of the PF is on the order of 100 km and has a mean downstream bottom-referenced U_{bcb} of 0.4 m s^{-1} at 500 m depth (taken from Figure 4 of *Foppert et al.* [2016]). A typical value of $\overline{V'T'}$ near the PF is about 0.01 m s^{-1} °C at 500 m depth (taken from Figure 10 of *Watts et al.* [2016]). This implies an increase in temperature on the order of 0.1°C along a 400 km path downstream of a major bathymetric ridge. This magnitude of temperature change may be observable with available hydrographic data (e.g. with Argo floats). Interestingly, *Foppert et al.* [2016] found, for relatively stable time periods, a depth-mean temperature difference of 0.3°C between a composite-mean PF upstream and downstream of the SFZ, some of which may be due to a convergence of $\overline{EHF}$ in the downstream jet.

The above posited increases in temperature at each of the $[\overline{EHF}]_{sat}$ hot spots are analogous to the deep changes in buoyancy found in the OFES model by *Thompson and Naveira-Garabato* [2014]. This increased temperature (or buoyancy) associated with lateral $[\overline{EHF}]_{sat}$ convergence is not able to interact with the atmosphere directly through air-sea flux, as it occurs throughout the water column. It must, therefore, be incorporated into the mean circulation of the ACC and leave the ACC laterally through mean heat flux associated with the overturning circulation (sometimes referred to as the Deacon cell). This is a topic of immediate interest, to both confirm the estimate of along-stream ΔT done here and to gain understanding of the relative importance of each hot spot of $[\overline{EHF}]_{sat}$.

4.4. Along-stream structure of $[\overline{EHF}]_{sat}$

In a broad sense, the locations of elevated $[\overline{EHF}]_{sat}$ correspond with where the $\overline{SSH}_{sat}$ contours pinch together (Figure 7a). This is especially apparent at the PAR where the latitudinal width between the SAF and the southern edge of the ACC reduces to less than half its upstream width before expanding again downstream, i.e. from more than 10° wide at 192°E to 4° wide at 215°E back to 10° wide by 232°E. *Thompson and Naveira-Garabato* [2014] find a similar pinching together and widening of mean streamlines associated with standing meanders set by steep bathymetry in the OFES model. The nearly flat sections of lines in Figure 7b, like that found in the Bellingshausen Basin ($220 - 290°$E), have a nearly inconsequential effect on the total $\oint[\overline{EHF}]_{sat}$. These are regions where *Thompson and Naveira-Garabato* [2014] showed a gradual steepening of buoyancy surfaces along the path of the ACC. These stretches of minimal $[\overline{EHF}]_{sat}$ accumulation can occur across the entire ACC, e.g. in the Bellingshausen Basin, or across a subset of $\overline{SSH}_{sat}$ contours. While $\oint[\overline{EHF}]_{sat}$ has nearly constant convergence south of the SAF (implied by the nearly constant slope in Figure 6a), when neighboring $\overline{SSH}_{sat}$ contours have different strengths of $[\overline{EHF}]_{sat}$, the convergence of heat between the streamlines is locally enhanced or reduced.

The relative contribution of heat to the total $\oint[\overline{EHF}]_{sat}$ at each hot spot depends on the $\overline{SSH}_{sat}$ contour, or path, chosen for integration. Western boundary current interactions are the prominent mechanism of $[\overline{EHF}]_{sat}$ across the northern streamlines of the ACC, whereas interactions with bathymetric features become increasingly important for the central and the southern streamlines. Figure 7b and Table 1 show the percentage of total $\oint[\overline{EHF}]_{sat}$ at each hot spot. The different relative contributions of each hot spot to the total $\oint[\overline{EHF}]_{sat}$ confounds extrapolation from local observations. Prior knowledge of the number of hot spots around the ACC band alone is not enough; it is also necessary to know the relative contribution of each. Additionally, some of the more influential hot spots have been relatively under studied or under observed. In particular, much focus has been on fluxes across the ACC in DP [e.g. *Watts et al.*, 2016; *Ferrari et al.*, 2014; *Bryden*, 1979], when, in fact, the BMC contributes a greater percentage of the total $\oint[\overline{EHF}]_{sat}$ across the northern flank of the ACC and the SAF, and contributes a greater absolute value of $[\overline{EHF}]_{sat}$ to the Southern Ocean heat budget than DP (Figure 7; Table 1).

That the percent of total $\oint[\overline{EHF}]_{sat}$ at each $[\overline{EHF}]_{sat}$ hot spot depends on the chosen $\overline{SSH}_{sat}$ implies a hand-off of heat between mean streamlines of the ACC (Figure 7b and Table 1). In other words, heat that enters the ACC through $[\overline{EHF}]_{sat}$ in the BMC or ARC is able to cross the next front when it encounters a subsequent $[\overline{EHF}]_{sat}$ hot spot downstream. Eventually, it can exit the ACC southward at, most likely, either the SWIR or KP. To the extent that $[\overline{EHF}]_{sat}$ is driven by baroclinic instability events that act to transport heat across strong upper water column fronts, the heat may cross the more quiescent regions of the ACC through another process, e.g. the mean heat flux due to the non-equivalent barotropic component of the velocity described by *Peña-Molino et al.* [2014].

Each region of elevated $[\overline{EHF}]_{sat}$ found in this study has its own unique properties of background mean flow and bathymetry that together set the amplitude of the standing meander. For example, the strongest $[\overline{EHF}]_{cDrake}$ found in *Watts et al.* [2016] is in the Polar Frontal Zone, an inter-frontal zone between the SAF and PF, where there are warm-core rings pinching off the SAF and cold-core rings pinching off the PF. *Chapman et al.* [2015] show that the amount of $\overline{EKE}$ produced and the amount of $\overline{EHF}$ (characterized by vertical wave activity flux) decrease with a decreasing amplitude of the standing meander. That is, the amount of $\overline{EHF}$ and $\overline{EKE}$ depends on the amplitude of the standing meander, forced by the unique configuration of bathymetry and mean flow, that triggers the baroclinic instability process. The extension to biological productivity is unclear, yet there have been observations that warm and cold core rings have different implications for chlorophyll distributions and primary production at the SWIR[*Ansorge et al.*, 2010]. Thus, it is crucial to have a good understanding of the background mean flow in order to quantify, and perhaps predict, the amount of $[\overline{EHF}]$ crossing the ACC locally at each hot spot and the implications thereof.

4.5. Temporal trends of $[EHF]_{sat}$

There has been discussion in recent literature about the ACC eddy field's response to increasing and poleward-shifting winds in the Southern Ocean [e.g. *Meredith and Hogg*, 2006; *Hogg et al.*, 2014; *Meredith*, 2016]. In this study, the long-term trend in low-frequency $[EHF]_{sat}$ in each hot spot is diagnosed in a running-mean sense using 4-year subsets of H^*_{sat} overlapped by 2 years (Figure 8). This reduces any variability occurring on time scales shorter than a few years, while retaining enough data to appropriately calculate trends. We find that the long-term trends from 1993 through 2014 vary in both sign and magnitude depending on location in the ACC, with only three of the eight $[\overline{EHF}]_{sat}$ hot spots showing significant trends of increasing poleward heat fluxes.

Hogg et al. [2014] find positive long-term linear trends in EKE from 1993 through 2012 in the Indian and Pacific sectors of the Southern Ocean, and no trend in the Atlantic, associated with intensifying circumpolar winds. Those authors define an Indian sector that includes the KP and part of SEIR, two regions where we find significant increases in $[\overline{EHF}]_{sat}$ magnitude (Figure 8b). The BMC, the other hot spot with a significant trend of increasing $[\overline{EHF}]_{sat}$ magnitude, is not included in the Atlantic sector defined by *Hogg et al.* [2014]. It is important to note that the trends in EKE represent trends in oceanic storm track intensity, and do not necessarily represent trends in EHF [*Treguier et al.*, 2010].

In other words, the eddies may persist longer with enhanced EKE, but the amount of baroclinic growth and EHF could remain the same or even decrease. *de Souza et al.* [2013] find an increase in southward heat flux, based on an eddy diffusivity parameterization from sea level anomaly and mean temperature gradient, equivalent to 0.78% yr^{-1} of the total across the circumpolar PF. While that trend was calculated over a 4-year record from 2006 through 2009, the magnitude of the trend as a percentage of the mean falls within the range of values from the $[\overline{EHF}]_{sat}$ hot spots presented in the legend of Figure 8b.

Table 1 shows that 47% of the total $\oint[\overline{EHF}]_{sat}$ that crosses the southern edge of the ACC occurs in the Indian sector of the Southern Ocean (i.e. at SWIR and KP). Recent findings have pointed out several source locations for Antarctic Bottom Water with up to 40% produced in the Indian Sector [e.g. *Jacobs*, 2004; *Meredith*, 2013]. The $[\overline{EHF}]_{sat}$ at SWIR and KP may act as direct sources of heat to the shelf and slope waters by baroclinic eddies. Both regions show large trends of $[EHF]_{sat}$ over the satellite record, respectively, of 0.26 MW m^{-1} and -0.27 MW m^{-1} (Figure 8). Note that the signs of these trends are opposite, with increasing $[EHF]_{sat}$ magnitude at KP and decreasing $[EHF]_{sat}$ magnitude at the SWIR. These changes in $[EHF]_{sat}$ could have consequences on amount of Antarctic Bottom Water formed in the Indian sector of the Southern Ocean.

5. Conclusion

SSH standard deviation (H^*) and time-mean, depth-integrated, divergent, downgradient eddy heat flux ($[\overline{EHF}]$) are related through a power law that is quantified using SOSE. The pattern of $[\overline{EHF}]_{sat}$ in the Southern Ocean estimated from satellite altimetry is strongly tied to large local bathymetric features and interactions with western boundary currents of the subtropical gyres. Heat enters the northern ACC from the subtropical gyres, mainly through interactions at the BMC and ARC, and appears to take a circuitous path before exiting the southern edge of the ACC. Pulses of $[\overline{EHF}]_{sat}$ occur at different locations along different $\overline{SSH}_{sat}$ contours. Integrated along circumpolar streamlines within the ACC band, $\oint[\overline{EHF}]_{sat}$ has a maximum value of 1.06 PW and a minimum of 0.02 PW, with an estimated uncertainty of 0.02 PW. This implies a convergence of heat due to eddies between circumpolar streamlines of the ACC, particularly for those north of the SAF. The values of $\oint[\overline{EHF}]_{sat}$ found here fall within the values of estimated from circumpolar extrapolation from local observations [e.g. *Watts et al.*, 2016; *Phillips and Rintoul*, 2000], found in model simulations [e.g. *Meijers et al.*, 2007; *Volkov et al.*, 2010], and calculated from float data [e.g. *Gille*, 2003; *Zhiwei et al.*, 2014].

Each region of elevated $[\overline{EHF}]_{sat}$ tied to ACC interactions with bathymetry has its own unique configuration of mean flow and bathymetry that sets the size of the standing meander and the strength of EHF. Significant long-term increases in $[EHF]_{sat}$ magnitude occurring at KP and SEIR may be related to the intensifying westerly winds over the ACC. On the other hand, the significant increases in $[EHF]_{sat}$ magnitude at the BMC and small insignificant trend of the opposite sign at the ARC are likely related to changes in the strength of the subtropical gyres and/or changes in water mass properties more so than to changes in circumpolar wind stress over the Southern Ocean. It could be suggested that if the major fronts of the ACC shift southward due to changes in the winds, the locations of direct sources of heat out of the ACC towards the Antarctic slope and shelf could change. That is, the shifted jets may have to negotiate different parts of the ridge systems with concomitant changes regarding where $[\overline{EHF}]_{sat}$ hot spots occur in the ACC and how much heat crosses the southern edge of the ACC due to eddies.

Acknowledgments. The authors are grateful for support from the National Science Foundation grants OCE1141802 and OCE1358470. The cDrake data are available at the National Centers for Environmental Information, online at http://www.nodc.noaa.gov. We thank M. Mazloff for his helpful comments and for providing us with auxiliary SOSE data; computational resources for the SOSE were provided by NSF XSEDE resource grant OCE130007. MATLAB codes and files for this manuscript can be found online at http://digitalcommons.uri.edu/physical_oceanography_techrpts/6/. We also thank two reviewers whose constructive comments helped to greatly improve this manuscript.

References

Abernathey, R. P., and P. Cessi (2014), Topographic enhancement of eddy efficiency in baroclinic equilibration, *Journal of Physical Oceanography*, *44*(8), 2107–2126, doi: http://dx.doi.org/10.1175/JPO-D-14-0014.1.

Abernathey, R. P., J. Marshall, M. R. Mazloff, and E. Shuckburgh (2010), Enhancement of mesoscale eddy stirring at steering levels in the Southern Ocean, *Journal of Physical Oceanography*, *40*(1), 170–184, doi:http://dx.doi.org/10.1175/2009JPO4201.1.

Abernathey, R. P., I. Cerovecki, P. R. Holland, E. Newsom, M. R. Mazloff, and L. D. Talley (2016), Water-mass transformation by sea ice in the upper branch of the Southern Ocean overturning, *Nature Geoscience*, doi:10.1038/ngeo2749.

Adcroft, A., J. R. Scott, and J. Marotzke (2001), Impact of geothermal heating on the global ocean circulation, *Geophysical Research Letters*, *28*, 1735–1738, doi: 10.1029/2000GL012182.

Ansorge, I. J., E. A. Pakhomov, S. Kaehler, J. R. E. Lutjeharms, and J. V. Durgadoo (2010), Physical and biological coupling in eddies in the lee of the South-West Indian Ridge, *Polar Biology*, *33*, 747–759, doi:10.1007/s00300-009-0752-9.

Bishop, S. P., D. R. Watts, and K. A. Donohue (2013), Divergent eddy heat fluxes in the Kuroshio Extension at 144 - 146E. Part I: Mean structure, *Journal of Physical Oceanography*, *43*(8), 1533–1550, doi:10.1175/JPO-D-12-0221.1.

Bryden, H. L. (1979), Poleward heat flux and conversion of available potential energy in Drake Passage, *Journal of Marine Research*, *37*, 1–22.

Chang, E. K. M., and I. Orlanski (1993), On the dynamics of a storm track, *Journal of the Atmospheric Sciences*, *50*(7), 999–1015.

Chapman, C. C., A. M. Hogg, A. E. Kiss, and S. R. Rintoul (2015), The dynamics of Southern Ocean storm tracks, *Journal of Physical Oceanography*, *45*(3), 884–903, doi:10.1175/JPO-D-14-0075.1.

Chereskin, T. K., K. A. Donohue, and D. R. Watts (2012), cDrake: Dynamics and transport of the Antarctic Circumpolar Current in Drake Pasage, *Oceanography*, *25*(3), 134–135, doi:http://dx.doi.org/10.5670/oceanog.2012.86.

Chidichimo, M. P., K. A. Donohue, D. R. Watts, and K. L. Tracey (2014), Baroclinic transport time series of the Antarctic Circumpolar Current measured in Drake Passage, *Journal of Physical Oceanography*, *44*, 1829–1853, doi:10.1175/JPO-D-13-071.1.

de Souza, J. M. A. C., A. d. M. Paiva, and K. Von Schuckmann (2013), New estimates for the heat flux across the Polar Front: spatial and temporal variability in recent years, *Antarctic Science*, *25*(3), 433–444, doi:10.1017/S0954102012001113.

de Szoeke, R. A., and M. D. Levine (1981), The advective flux of heat by mean geostrophic motions in the Southern Ocean, *Deep Sea Researh I*, *28*, 1057–1085.

Donohue, K. A., M. A. Kennelly, and A. Cutting (2016), Sea surface height variability in Drake Passage, *Journal of Atmospheric and Oceanic Technology*, *33*(4), 669–683, doi:10.1175/JTECH-D-15-0249.1.

Ferrari, R., and M. Nikurashin (2010), Suppression of eddy diffusivity across jets in the Southern Ocean, *Journal of Physical Oceanography*, *40*(7), 1501–1519, doi: http://dx.doi.org/10.1175/2010JPO4278.1.

Ferrari, R., C. Provost, Y.-H. Park, N. Sennéchael, Z. Koenig, H. Sekma, G. Garric, and R. Bourdallé-Badie (2014), Heat fluxes across the Antarctic Circumpolar Current in Drake Passage: Mean flow and eddy contributions, *Journal of Geophysical Research: Oceans*, *119*, 6381–6402, doi:10.1002/2014JC010201.

Firing, Y. L., T. K. Chereskin, D. R. Watts, K. L. Tracey, and C. Provost (2014), Computation of geostrophic streamfunction, its derivatives, and error estimates from an array of CPIES in Drake Passage, *Journal of Atmospheric and Oceanic Technology*, *31*, 656–680, doi:10.1175/JTECH-D-13-00142.1.

Foppert, A., K. A. Donohue, and D. R. Watts (2016), The Polar Front in Drake Passage: A composite-mean stream-coordinate view, *Journal of Geophysical Research: Oceans*, *121*, 1771–17,881, doi:10.1002/2015JC011333.

Gille, S. T. (2003), Float observations of the Southern Ocean. Part II: Eddy fluxes, *Journal of Physical Oceanography*, *33*(6), 1182–1196, doi:10.1175/1520-0485(2003)033¡1182:FOOTSO¿2.0.CO;2.

Hogg, A. M., M. P. Meredith, D. P. Chambers, E. P. Abrahamsen, C. W. Hughes, and A. K. Morrison (2014), Recent trends in the Southern Ocean eddy field, *Journal of Geophysical Research: Oceans*, *120*, 257–267, doi:10.1002/2014/JC010470.

Holloway, G. (1986), Estimation of oceanic eddy transports from satellite altimetry, *Nature*, *323*, 243–244, doi:10.1038/323243a0.

Jacobs, S. S. (2004), Bottom water production and its links with the thermohaline circulation, *Antarctic Science*, *16*(4), 427–437, doi:10.1017/S095410200400224X.

Karsten, R. H., and J. Marshall (2002), Constructing the residual circulation of the ACC from observations, *Journal of Physical Oceanography*, *32*(12), 3315–3327, doi: 10.1175/1520-0485(2002)032¡3315:CTRCOT¿2.0.CO;2.

Keffer, T., and G. Holloway (1988), Estimating Southern Ocean eddy flux of heat and salt from satellite altimetry, *Nature*, *332*, 624–626, doi:10.1038/332624a0.

Kushner, P. J., and I. M. Held (1998), A test, using atmospheric data, of a method for estimating oceanic eddy diffusivity, *Geophysical Research Letters*, *25*(22), 4213–4216, doi:10.1029/1998GL900142.

Large, W. G., and A. J. Nurser (2001), *Ocean Circulation and Climate: Observing and Modeling the Global Ocean*, Academic Press.

Levitus, S. (1987), Meridional Ekman heat fluxes for the world ocean and individual ocean basins, *Journal of Physical Oceanography*, *17*(9), 1484–1492, doi: http://dx.doi.org/10.1175/1520-0485(1987)017¡1484:MEHFFT¿2.0.CO;2.

Marshall, G. J. (2003), Trends in the Southern Annular Mode from observations and reanalyses, *Journal of Climate*, *16*, 4134–4143, doi:10.1175/1520-0442(2003)016¡4134:TITSAM¿2.0.CO;2.

Marshall, J., and G. Shutts (1981), A note on rotational and divergent eddy fluxes, *Journal of Physical Oceanography*, *11*, 1677–1680, doi:10.1175/1520-0485(1981)011¡1677:ANORAD¿2.0.CO;2.

Marshall, J., E. Shuckburgh, H. Jones, and C. Hill (2006), Estimates and implications of surface eddy diffusivity in the Southern Ocean derived from tracer transport, *Journal of Physical Oceanography*, *36*(9), 1806–1821, doi:http://dx.doi.org/10.1175/JPO2949.1.

Masich, J., T. K. Chereskin, and M. R. Mazloff (2015), Topographic form stress in the Southern Ocean State Estimate, *Journal of Geophysical Research: Oceans*, *120*, 7919–7933, doi:10.1002/2015JC011143.

Mazloff, M. R., P. Heimbach, and C. Wunsch (2010), An eddy-permitting Southern Ocean State Estimate, *Journal of Physical Oceanography*, *40*(5), 880–899, doi:10.1175/2009JPO4236.1.

Meijers, A. J., N. L. Bindoff, and J. L. Roberts (2007), On the total, mean, and eddy heat and freshwater transports in the Southern Hemisphere of a 1/8 x 1/8 global ocean model, *Journal of Physical Oceanography*, *37*(2), 277–295, doi:10.1175/JPO3012.1.

Meredith, M. P. (2013), Replenishing the abyss, *Nature Geoscience*, *6*, 166–167, doi:10.1038/ngeo1743.

Meredith, M. P. (2016), Understanding the structure of changes in the Southern Ocean eddy field, *Geophysical Research Letters*, *43*, 5829–5832, doi:10.1002/2016GL069677.

Meredith, M. P., and A. M. Hogg (2006), Circumpolar response of Southern Ocean eddy activity to a change in the Southern Annular Mode, *Geophysical Research Letters*, *33*, L16,608, doi:10.1029/2006GL026499.

Pedlosky, J. (1987), *Geophysical Fluid Dynamics*, 2cd ed., Springer-Verlag.

Peña-Molino, B., S. R. Rintoul, and M. R. Mazloff (2014), Barotropic and baroclinic contributions to along-stream and across-stream transport in the Antarctic Circumpolar Current, *Journal of Geophysical Research: Oceans*, *119*, 8011–8028, doi: 10.1002/2014JC010020.

Phillips, H. E., and S. R. Rintoul (2000), Eddy variability and energetics from direct current measurements in the Antarctic Circumpolar Current south of Australia, *Journal of Physical Oceanography*, *30*(12), 3050–3076, doi:10.1175/1520-0485(2000)030¡3050:EVAEFD¿2.0.CO;2.

Sekma, H., Y.-H. Park, and F. Vivier (2013), Time-mean flow as the prevailing contributiont to the poleward heat flux across the southern flank of the Antarctic Circumpolar Current: A case study in the Fawn Trough, Kerguelen Plateau, *Journal of Physical Oceanography*, *43*(3), 583–601, doi:10.1175/JPO-D-12-0125.1.

Smith, W. H., and D. T. Sandwell (1997), Global sea floor topography from satellite altimetry and ship depth soundings, *Science*, *277*(5334), 1956–1962, doi: 10.1126/science.277.5334.1956.

Thompson, A. F., and A. C. Naveira-Garabato (2014), Equilibration of the Antarctic Circumpolar Current by standing meanders, *Journal of Physical Oceanography*, *44*(7), 1811–1828, doi:10.1175/JPO-D-13-0163.1.

Thompson, A. F., and J.-B. Sallée (2012), Jets and topography: Jet transitions and the impact on transport in the Antarctic Circumpolar Current, *Journal of Physical Oceanography*, *42*(6), 956–972, doi:10.1175/JPO-D-11-0135.1.

Tracey, K. L., K. A. Donohue, D. R. Watts, and T. K. Chereskin (2013), cDrake CPIES data report November 2007 to December 2011, *GSO Technical Report Paper 4*, University of Rhode Island Physical Oceanography.

Treguier, A. M., J. Le Sommer, J. M. Molines, and B. de Cuevas (2010), Response of the Southern Ocean to the Southern Annular Mode: Interannual variability and multidecadal trend, *Journal of Physical Oceanography*, *40*(7), 1659–1668, doi: 10.1175/2010JPO4364.1.

Volkov, D. L., L.-L. Fu, and T. Lee (2010), Mechanisms of the meridional heat transport in the Southern Ocean, *Ocean Dynamics*, *60*, 791–801, doi:10.1007/s10236-010-0288-0.

Watts, D. R., K. L. Tracey, K. A. Donohue, and T. K. Chereskin (2016), Estimates of eddy heat flux crossing the Antarctic Circumpolar Current from observations in Drake Passage, *Journal of Physical Oceanography*, *46*(7), 2103–2122, doi:10.1175/JPO-D-16-0029.1.

Zhiwei, Z., Z. Yisen, T. Jiwei, Y. Qingxuan, and Z. Wei (2014), Estimation of eddy heat transport in the global ocean from Argo data, *Acta Oceanologica Sinica*, *33*(1), 42–47, doi:10.1007/s13131-014-0421-x.

Table 1. $[\overline{EHF}]_{sat}$ at hot spots of eddy activity along 5 $\overline{SSH}_{sat}$ contours[a]

Label	$\overline{SSH}_{sat}$ [m]	ARC	BMC	SWIR	KP	SEIR	MR	PAR	DP	total [PW]
N-Edge	0.3	42	47	–	–	5	–	1	–	-1.06
SAF	-0.1	14	27	1	6	16	14	4	12	-0.33
PF	-0.4	1	13	15	6	15	12	6	23	-0.24
SACCF	-0.8	–	7	22	21	15	3	6	15	-0.08
S-Edge	-1.0	–	11	26	21	7	3	9	7	-0.02

[a] Hot spot values presented as a percent of the total circumpolar path-integrated values (last column). Hot spots with less than 0.5% of the total $\oint[\overline{EHF}]_{sat}$ are left empty. All regions are defined by their longitudinal limits shown in Figure 7b. The SWIR, ARC and KP have additional latitudinal limits, as do DP and BMC, so that there is no overlap between regions. See text for abbreviations (Section 3.2).

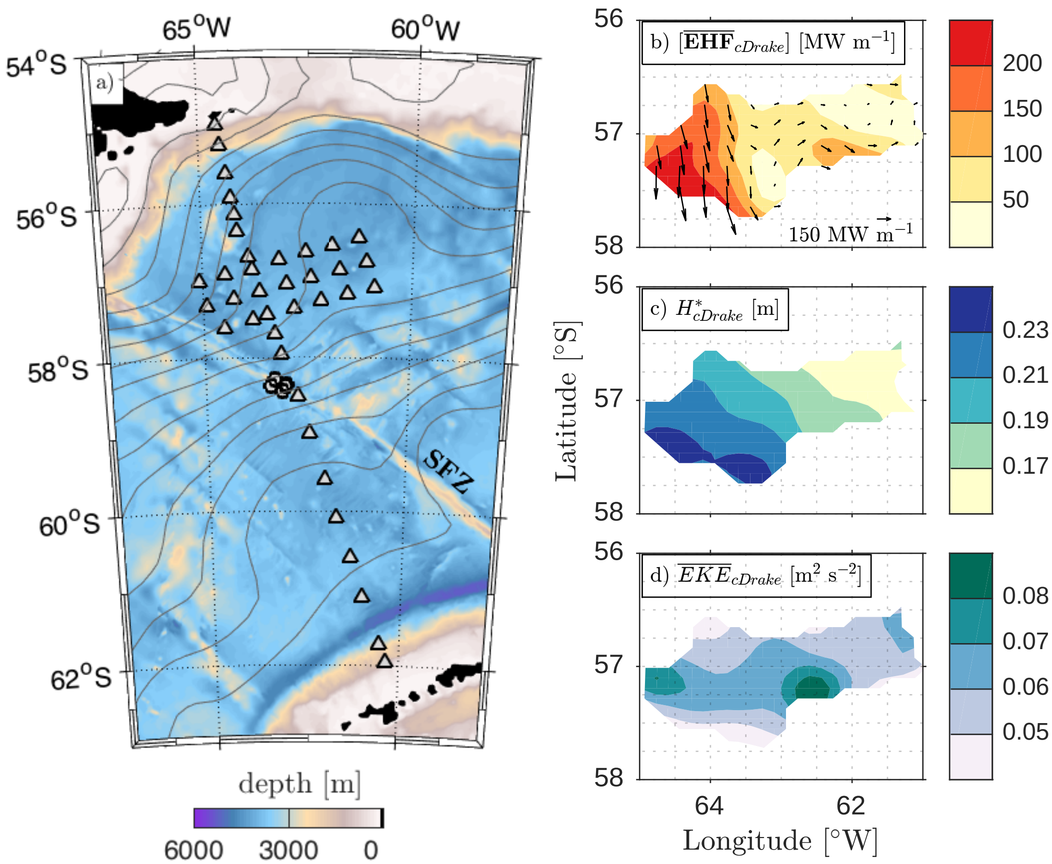

Figure 1. cDrake results. (a) Map of bathymetry [m] from *Smith and Sandwell* [1997] merged with multi-beam data (filled color contours) and the cDrake array of CPIES (triangles) in Drake Passage. The submarine ridge spanning Drake Passage, the Shackleton Fracture Zone (SFZ) is labelled in the southern passage. The circles represent the subset of CPIES deployed in the final year of the experiment. The nearly 23.5-year mean SSH field (described in Section 2.3) is shown as gray lines with a contour interval of 0.1 m. (b) $[\overline{\boldsymbol{EHF}}]_{cDrake}$ [MW m^{-1}]: 4-year mean depth-integrated (surface to 3500 m) eddy heat flux magnitude from the mapped CPIES variables with a contour interval of 50 MW m^{-1}. The arrows indicate the direction of $[\overline{\boldsymbol{EHF}}]_{cDrake}$ at every other point on the mapped grid. (c) H^*_{cDrake} [m]: SSH_{cDrake} standard deviation over the 4 years, from 2007 through 2011, with a contour interval of 0.02 m. (d) $\overline{EKE}_{cDrake}$ [m^2 s^{-2}]: 4-year mean surface eddy kinetic energy with contour interval of 0.01 m^2 s^{-2}.

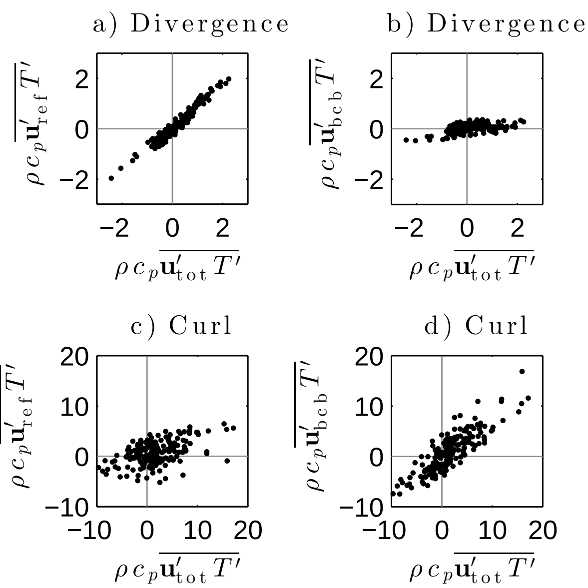

Figure 2. Divergence (a,b) and curl (c,d) of total EHF ($\rho c_p \overline{\boldsymbol{u}'_{tot} T'}$) compared to the reference EHF ($\rho c_p \overline{\boldsymbol{u}'_{ref} T'}$) and baroclinic EHF ($\rho c_p \overline{\boldsymbol{u}'_{bcb} T'}$) at 400 m depth within the local dynamics array of CPIES in Drake Passage in units of W m^{-3}. The total EHF on the x-axis is plotted against the reference EHF (a,c) and baroclinic EHF (b,d) on the y-axis.

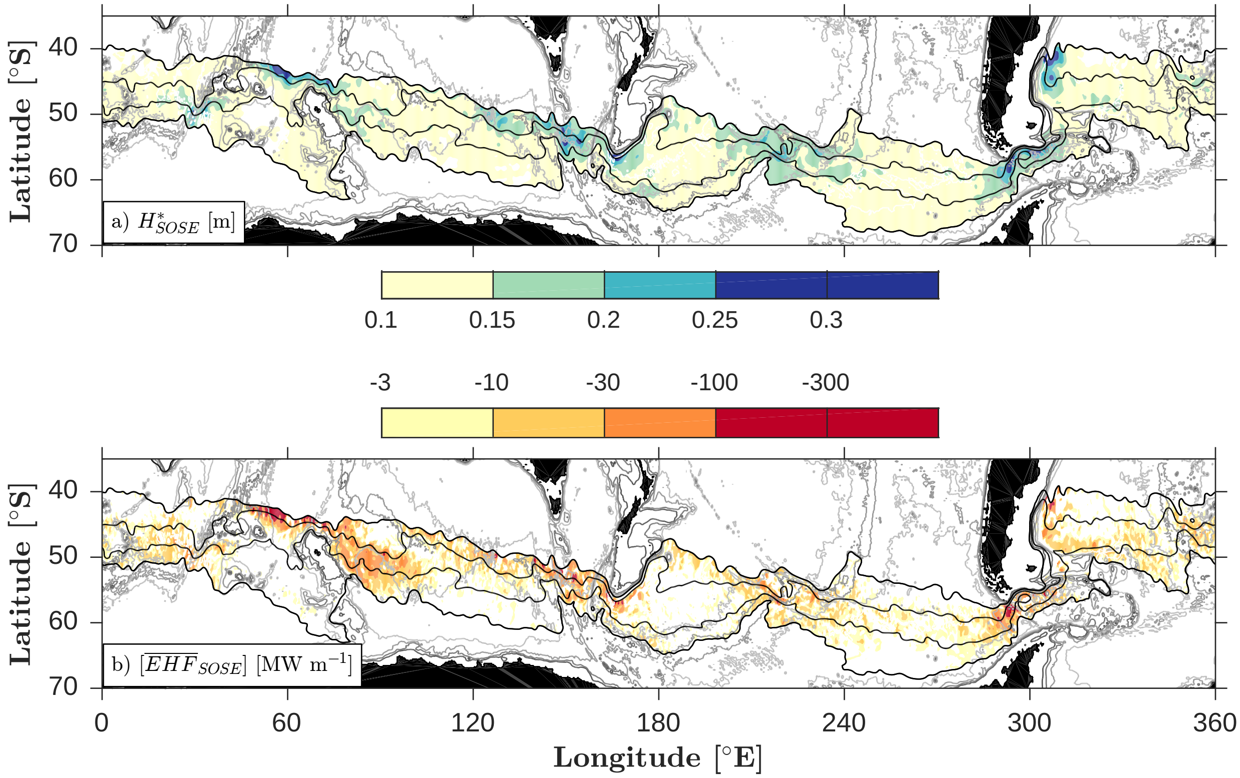

Figure 3. SOSE maps of the Southern Ocean with model depth contoured every 1000 m in gray and mean circumpolar streamlines defining outer edges of the ACC band ($\overline{SSH}_{SOSE} = -0.8$ to 0.2 m) and two more central contours ($\overline{SSH}_{SOSE} = -0.5$ and -0.1 m) in black. (a) H^*_{SOSE} [m]: daily SSH_{SOSE} standard deviation over the 6 years of SOSE Iteration 100, from 2005 through 2010. Values less than 0.1 m are left unshaded and those greater than 0.25 m are dark blue. Note that all values greater than 0.3 m are only found in the Agulhas Return Current and Brazil-Malvinas Confluence regions. (b) $[\overline{EHF}]_{SOSE}$ [MW m^{-1}]: time-mean depth-integrated (surface to 2000 m) cross-frontal eddy heat flux calculated in SOSE. Only negative (i.e. down gradient) values are plotted. Values with a magnitude less than 3 MW m^{-1} are left unshaded and those greater than 100 MW m^{-1} are dark red. Note that all values greater than 300 MW m^{-1} are only found in the Agulhas Return Current and Brazil-Malvinas Confluence regions.

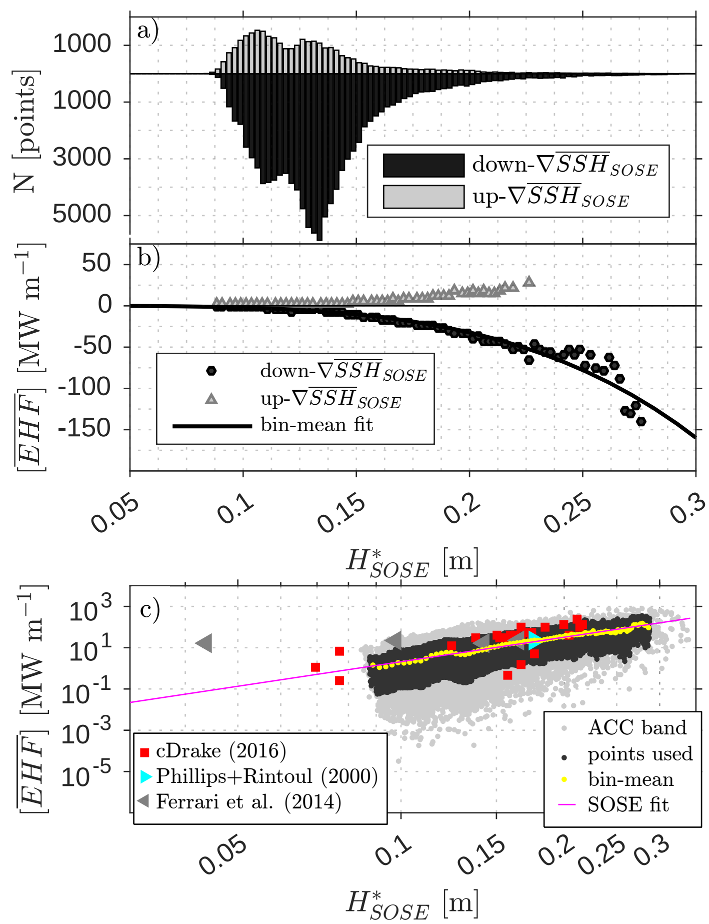

Figure 4. (a) Cross-frontal eddy heat flux calculated in SOSE, $[\overline{EHF}]_{SOSE}$, as a function of SSH_{SOSE} standard deviation, H^*_{SOSE} [m], within the ACC band of mean streamlines ($\overline{SSH}_{SOSE} = -0.8$ to 0.2 m). Gray/black bars indicate a heat flux up/down the $\overline{SSH}_{SOSE}$ gradient. (b) $[\overline{EHF}]_{SOSE}$ [MW m^{-1}] averaged within 0.025 m-wide H^*_{SOSE} bins. Upgradient (gray triangles) and downgradient (black circles) $[\overline{EHF}]_{SOSE}$ are averaged independently and only bins containing greater than 30 points are considered. The black line represents the bin-averaged power-law fit used in this study. (c) Downgradient $[\overline{EHF}]$ values as a function of H^* from several sources are plotted on a log-log scale. Points from SOSE within the ACC used for the bin-averaged fit (black dots), points considered outliers (light gray dots), and bin-averaged points (yellow dots) are all shown. The magenta line represents the bin-mean power-law fit (Equation 4). cDrake points (red squares) and other significant observations of $[\overline{EHF}]$ in the ACC (triangles) are plotted as a function of H^*_{sat} over their respective time periods.

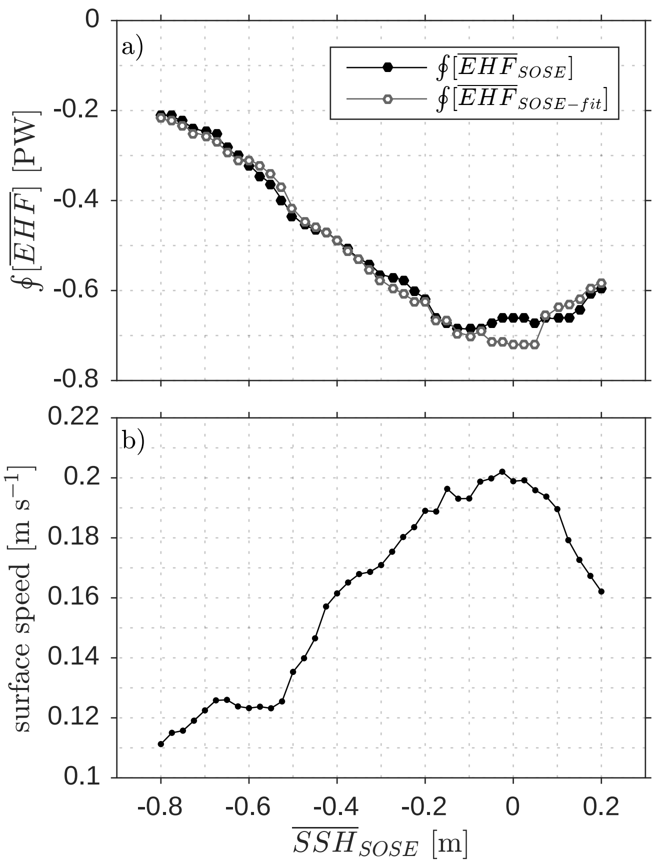

Figure 5. (a) Circumpolar path-integrated $\oint[\overline{EHF}]$ [PW= 10^{15} W] calculated directly in SOSE ($\oint[\overline{EHF}]_{SOSE}$; black filled circles) and estimated from the bin-averaged power law fit to H^*_{SOSE} ($\oint[\overline{EHF}]_{SOSE-fit}$; gray open circles). Negative values indicate a flux in the downgradient direction, i.e. towards Antarctica and the southern seas. (b) Mean geostrophic speed [m s^{-1}] at 5 m depth along circumpolar $\overline{SSH}_{SOSE}$ contours.

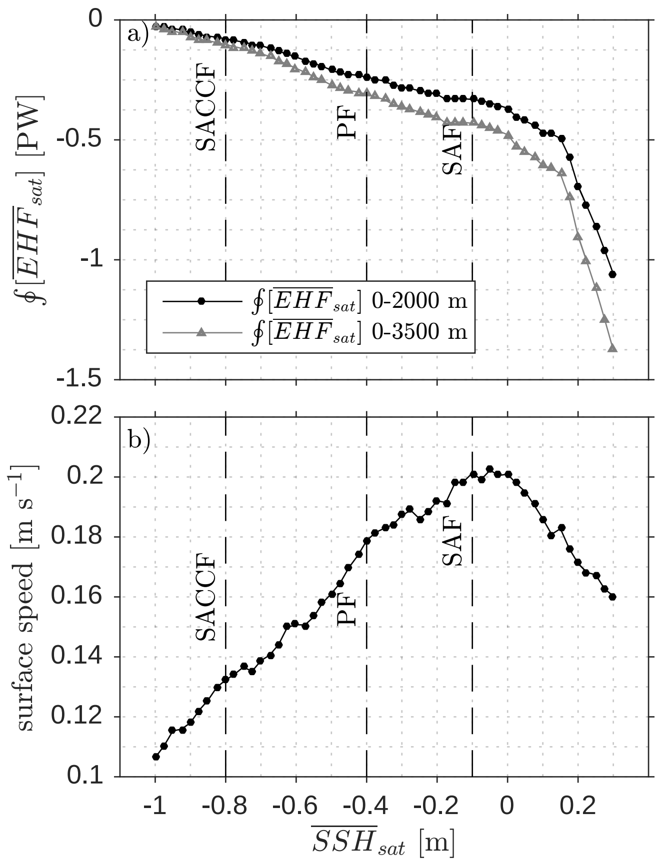

Figure 6. (a) $\oint[\overline{EHF}]_{sat}$ [PW] estimated from H^{*}_{sat} over the full-length (nearly 23.5 years) record of SSH_{sat} using the Southern Ocean power law in Equation 4 (black circles). The estimate is scaled up using the average ratio of surface-to-2000 m to surface-to-3500 m $[\overline{EHF}]_{cDrake}$ of 1.3 to a full-depth, i.e. surface to 3500 m, integration (gray triangles). (b) Mean surface geostrophic speed [m s^{-1}] along circumpolar $\overline{SSH}_{sat}$ contours. Nominal positions of the major fronts of the ACC are labelled.

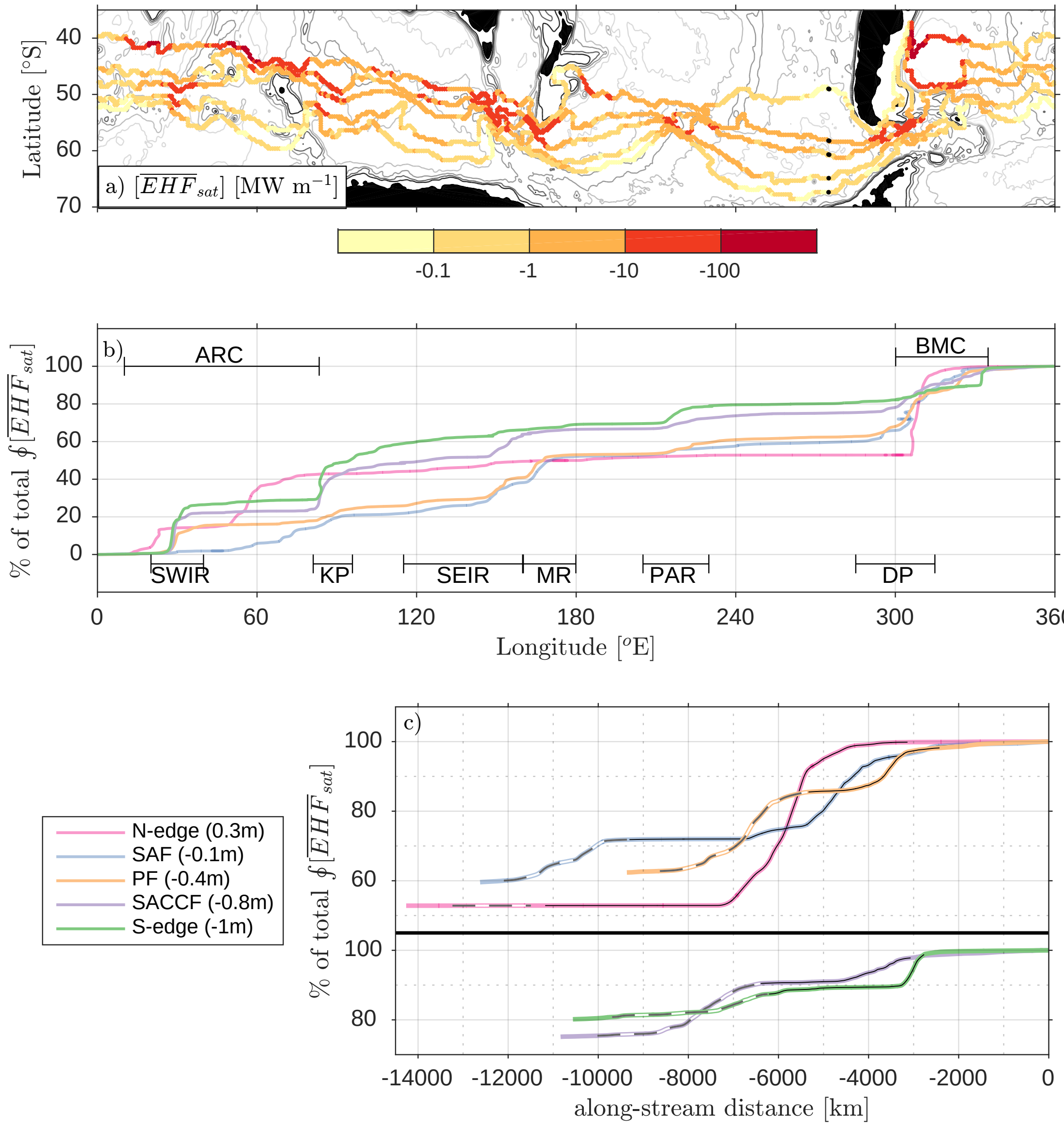

Figure 7. (a) $[\overline{EHF}]_{sat}$ [MW m^{-1}] along circumpolar streamlines. (b) Cumulative percent of total $\oint[\overline{EHF}]_{sat}$ along the five $\overline{SSH}_{sat}$ contours in panel (a) as a function of longitude. Longitudinal ranges of the eight $[\overline{EHF}]_{sat}$ hot spots are denoted by the horizontal bars and labelled. (c) An alternative view of the DP and BMC regions: cumulative percent of total $\oint[\overline{EHF}]_{sat}$ along the $\overline{SSH}_{sat}$ contours in panel (a), with the three northern streamlines in upper panel and the two southern streamlines in lower panel, as a function of along-stream distance east of 275°E (black dots in (a)), such that 0 km is 360°E. Within the colored lines, the DP region is designated by the thin white and gray dashed line and the BMC region is designated by the thin solid black line.

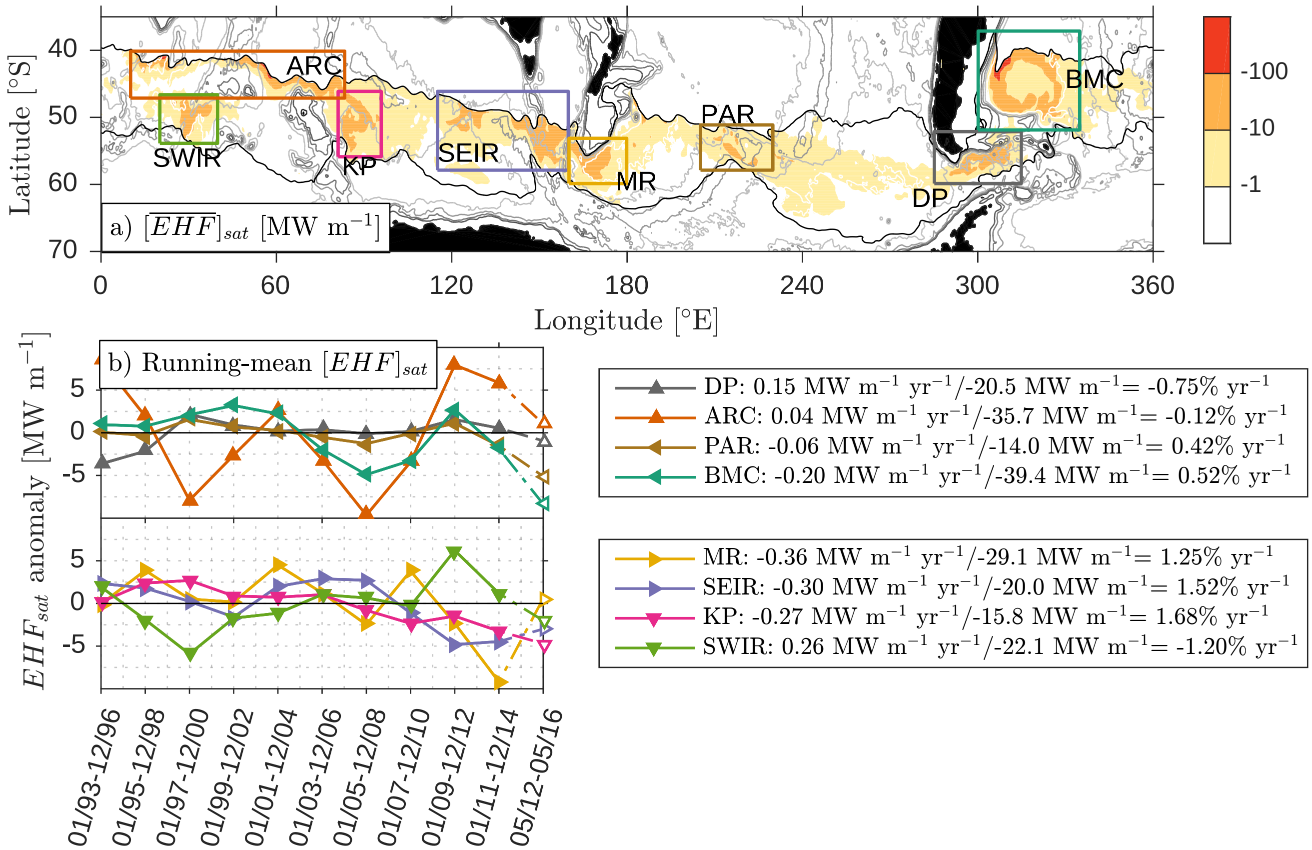

Figure 8. (a) Map of $[\overline{EHF}]_{sat}$ [MW m^{-1}]. The eight hot spots of $[\overline{EHF}]_{sat}$ are designated by the colored boxes and labelled. (b) Time series of running-mean $[EHF]_{sat}$ anomaly averaged over points within each box where $[\overline{EHF}]_{sat} \leq -10$ MW m^{-1}. Each colored line represents a particular $[\overline{EHF}]_{sat}$ hot spot and the colors are consistent with the colored boxes identifying the different regions in panel (a). The legends list the slope of the linear regression divided by the regional mean (using points where $[\overline{EHF}]_{sat} \leq -10$ MW m^{-1}) to express each as a percent per year for each hot spot. KP, SEIR, and BMC are the regions with statistically significant trends.

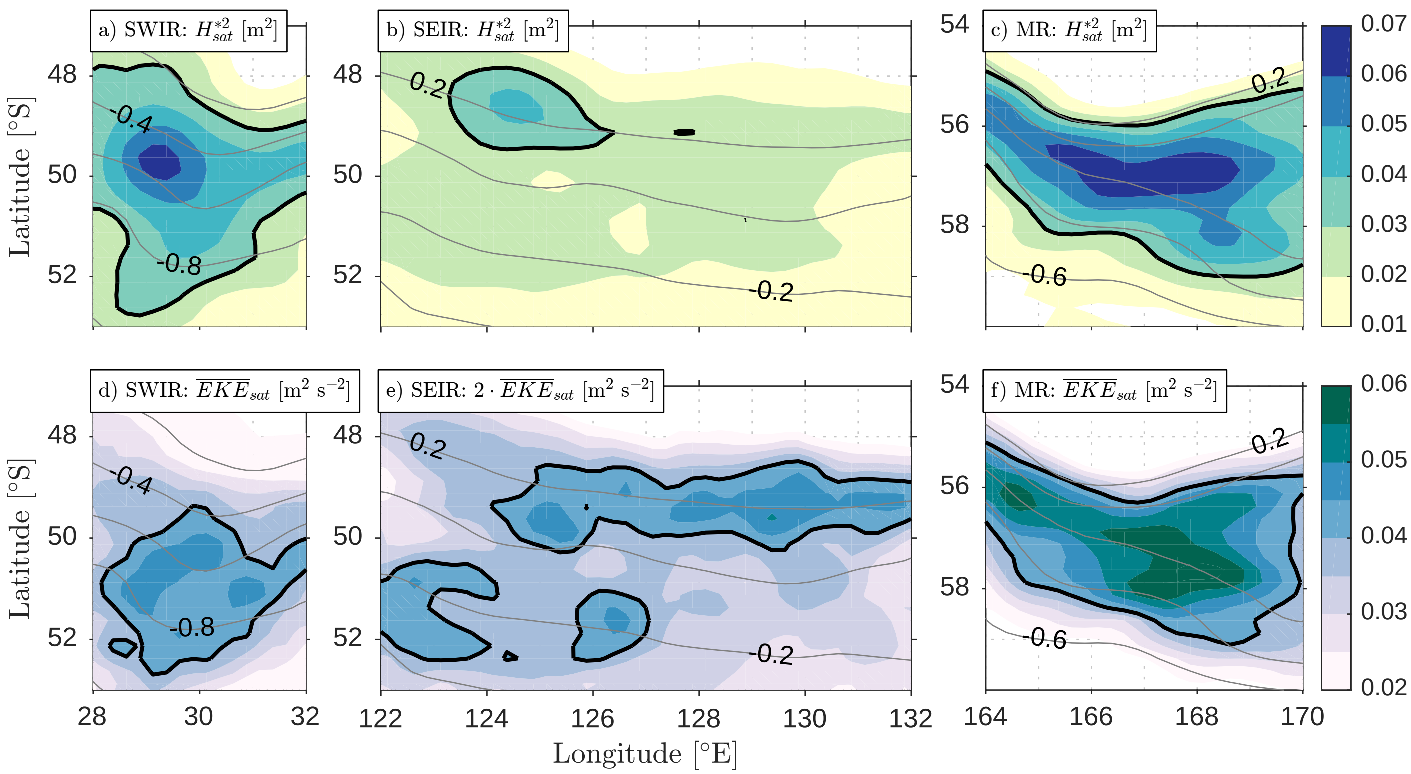

Figure 9. Observations of oceanic storm tracks highlighting the spatial offset between H^{*2}_{sat} [m^2] (a–c) and $\overline{EKE}_{sat}$ [m^2 s^{-2}] (d–f) in a subsection of three $[\overline{EHF}]_{sat}$ hotspots: Southwest Indian Ridge, Southeast Indian Ridge, and Macquarie Ridge (SWIR, SEIR, and MR). Note that H^{*2}_{sat} is presented here because it is more similar unit-wise to EPE than H^{*}_{sat}, and thus more analogous to $\overline{EKE}$. The contour interval for H^{*2}_{sat} is 0.01 m^2 and the$H^{*2}_{sat} = 0.03$ m^2 contour in black. The contour interval for $\overline{EKE}_{sat}$ is 0.005 m^2 s^{-1}, with $\overline{EKE}_{sat} = 0.04$ m^2 s^{-2} in black. Note also that we present $2 \cdot \overline{EKE}_{sat}$ in the region within the SEIR (panel e), so that we can use consistent colorbar limits. Therefore, the black line represents $\overline{EKE}_{sat} = 0.02$ m^2 s^{-2} in the SEIR region. The gray contour lines overlaid in each panel represent $\overline{SSH}_{sat}$ with a contour interval of 0.2 m and values are given by the numeric label.